WILEY | Hindawi

Research Article

Enhancing the Efficiency of Inverted Organic Solar Cells with Treatment Techniques: Numerical and Experimental Study

Davoud Raeyani [1,2] and Asghar Asgari [1,2,3]

^{1}*Faculty of Physics, University of Tabriz, Tabriz 51665-163, Iran*
^{2}*Photonics Devices Research Group, Research Institute of Applied Physics and Astronomy, University of Tabriz, Tabriz 51665-163, Iran*
^{3}*School of Electrical, Electronic, And Computer Engineering, University of Western Australia, Crawley, WA 6009, Australia*

Correspondence should be addressed to Asghar Asgari; asgari@tabrizu.ac.ir

The combination of UV-ozone and Al-doping enhancements in the ZnO ETL layer was studied for fullerene-based (P3HT:PCBM) and nonfullerene-based (J71:m-ITIC) solar cells. The study focused on morphological and interfacial defects and their relation to the electrical and optical properties of different Al-doped ZnO layers. The study also investigated the surface recombination velocity at the interface of the ZnO/active layer, as well as the carrier lifetime and diffusion length of the active layer theoretically. The most effective Al-doping dosage was 3% for P3HT:PCBM and 2% for J71:m-ITIC, attributed to the varying sensitivity of the active layer materials to morphological enhancement.

1. Introduction

Organic photovoltaics (OPVs), one of the renewable energy sources, have attracted significant attention in the past two decades owing to their lightweight, flexible, and solution-processable properties [1–4]. Also, due to the use of low-cost materials in OPVs, they are known as an alternative to expensive silicon-based solar cells [5]. Bulk heterojunction (BHJ) and bilayer are the two primary types of OPVs, which have been studied extensively in the past few years [6, 7]. BHJ is a better structural design due to organic materials' limited exciton diffusion length [8]. It insinuates that a self-assembled mixture of donor and acceptor molecules improved charge transfer by limiting the exciton diffusion passways [9]. Also, the solution-processed layer-by-layer (LBL) structure as an alternative deposition method achieved high-performance parameters in OPVs [10, 11]. The LBL design takes advantage of the vertical phase separation between the donor and acceptor layers. The great challenge for this structure is exciton dissociation efficiency, which was recently enhanced by incorporating donors into the acceptor layer [8]. According to previous studies, the most efficient combination of organic donor and acceptor materials resulted in a maximum efficiency of 19% [9].

Despite the active layer structural and material modifications [12], some studies focused on boosting the properties of the transport layer and electrodes [13, 14]. Up to now, many materials have been used as the transport layer, including polymer [15], two-dimensional [16, 17], metal oxide [18], and quantum dots [19]. Metal oxide materials, including zinc oxide (ZnO) [20–22], TiO_2 [23–25], and SnO_2 [26–28], widely served as a low-cost, air-stable, and optically transparent electron transport layer (ETL) compared to their organic counterparts [29, 30]. ZnO is a good candidate for photovoltaic application because of better electron mobility [31] and is used chiefly in the so-called inverted architecture of OPVs [32].

Although ZnO has many favorable properties, it has some drawbacks. The surface defects presented on ZnO nanofilms can trap many carriers in the interface between the active layer and ETL. Passivating these defects can even show better performance for the ZnO layer [33, 34]. Oxygen

vacancies (V_o) and oxygen interstitial species (O_i) [35] are the defects that influence the optoelectronic and grain boundary properties of ZnO [36, 37]. These defects can affect the current density characteristics of OPVs [38–40].

Previous studies have tried various methods to neutralize ZnO layer defects, such as applying UV-ozone treatment [39–41], plasma treatment [42, 43], doping [44–47], chemical functionalizing [48–50], annealing [51], and incorporating Interfacial layers [52–54]. These methods successfully passivated the V_o defects and raised the OPV efficiency. However, the benefits of employing multiple techniques and analyzing their collective impact on solar cells have yet to be fully explored. Also, the optimal parameters for these methods and the ideal state for each process may differ based on the active layer material utilized. There are limited experimental and theoretical studies published on this subject.

Also, the nanoscale morphology of the active layer plays a crucial role in determining the performance of BHJ organic photovoltaic cells [55]. The phase separation, domain size, molecular orientation, and π-π stacking of organic molecules are critical morphological features determining solar cell efficiency [56]. Morphology-induced defects can lead to significant issues such as increasing recombination rates, reducing carrier mobility [55], and hindering charge separation [57]. Various factors influence these defects, including solvent selection [58], thermal annealing [59], donor-to-acceptor ratios [60], material concentration [61], and the use of additives [62]. Also, the substrate's surface texture may play a critical function in shaping the morphology of the BHJ layer [63]. The roughness and hydrophobicity of the substrate influence the morphology of the upper layer. The impact of substrates on morphology also relies on the molecular geometry of the system. For instance, in fullerene solar cells, the acceptor molecules have a spherical shape, facilitating phase separation and less susceptibility to morphological challenges. In contrast, non-fullerene acceptors with planar shapes may be more effective in driving phase separation [56]. To our knowledge, few studies have investigated the impact of transport layer treatments on defect states related to active layer morphological imperfections, both experimentally and theoretically.

In this work, we applied the Al-doping and the UV-ozone treatment techniques to enhance the performance of the ZnO layer in the inverted organic solar cells. In detail, we chose (poly(3-hexylthiophene-2,5-diyl) (P3HT): [6,6]-phenyl-C61-butyric acid methyl ester (PCBM) as fullerene solar cell and poly[[5,6-difluoro-2-(2-hexyldecyl)-2H-benzotriazole-4,7-diyl]-2,5-thiophenediyl[4,8-bis[5-(tripropylsilyl)-2-thienyl]benzo[1,2-b:4,5-b']dithiophene-2,6-diyl]-2,5-thiophenediyl] (J71): 3,9-bis(2-methylene-((3-(1,1-dicyanomethylene)-6/7-methyl)-indanone))-5,5,11,11-tetrakis(4-hexylphenyl)dithieno[2,3-d:2′,3′-d′]-s-indaceno[1,2-b:5,6-b']dithiophene (m-ITIC) as a nonfullerene solar cell. The adopted UV-ozone method is a simple approach compared to other surface treatment techniques using a UV lamp and O_2 gas flow. Solution-processable doping of aluminum is also a straightforward and cost-effective method achieved by adding aluminum salt to a zinc acetate solution. The main impetus of this research was to apply these treatments and to investigate their effects on zinc oxide trap levels and interface effects, as well as their impact on the morphological traps of the active layer. Figure 1 shows the schematic diagram representing this work. We used X-ray diffraction (XRD) spectroscopy, scanning electron microscopy (SEM), and atomic force microscopy (AFM) to investigate the grain size and surface morphology of the ZnO layer. We investigated the optoelectronic properties of the ZnO layer using UV-Vis absorption and photoluminescence (PL) spectroscopy. The electrical properties of ZnO nanofilms were studied using a four-point probe (4PP) measurement and electrochemical impedance spectroscopy (EIS) spectroscopy. We utilized contact angle analysis to explore the surface energy of the ZnO layer. Furthermore, we performed a simulation study through SCAPS software to understand how Al doping impacts the trap states in the active layer and the interface of the ZnO/active layer.

2. Experimental Details

2.1. Materials. Zinc acetate dehydrate (ZnAc, 99%) was purchased from Sigma Aldrich. 2-Ethanolamine (99%) was purchased from Samchun. PCBM, P3HT, and m-ITIC were obtained from Lumtec Corporation. J71 was acquired from Betterchem. Aluminum nitrate nonahydrate ($Al(NO_3)_3.9H_2O$) (99%), ethanol (99.9%), chloroform, dichlorobenzene, and MoO_3 were purchased from Merck. We used all chemicals directly without any further purification.

2.2. Device Fabrication. ITO glass substrates were cleaned in detergent, deionized water, acetone, and isopropyl alcohol using an ultrasonic bath. Then, oxygen plasma treatment was performed on substrates for 10 min. Aluminum nitrate nonahydrate was added in a different weight ratio to ZnAc while preparing the ZnO ethanol solution [40]. The ZnO solution was spin coated on ITO substrate at 2000 rpm and annealed at 150°C for 30 min. Subsequently, the ZnO layer was surface treated using the UV-ozone method for 0, 10, 20, and 30 s. The substrates moved to a nitrogen-filled glove box afterward. The BHJ blends were prepared in optimal weight ratios of 1 : 1.2 for J71:m-ITIC and 1 : 0.8 for P3HT:PCBM [64, 65]. The J71:m-ITIC was dissolved in chloroform and spin coated at 2000 rpm without annealing. In contrast, P3HT:PCBM was dissolved in dichlorobenzene and spin coated at 700 rpm. Then, they were annealed at 110°C for 10 min. Finally, we used thermal evaporation to deposit 15 nm of MoO_3 and 120 nm of silver.

2.3. Characterization. The current-voltage characteristics were measured using the Keithley 2410 source meter. For the sun simulation light source, we used a SIM-1030 IRA-SOL solar simulator (AM 1.5G, 100 mW.cm^{-2}). The external quantum efficiency (EQE) characteristics were measured using the IRASOL IPCE-015 equipment. The UV-Vis absorption and photoluminescence spectra were measured using a Shimadzu UV-2450 UV-visible spectrophotometer and a JASCO FP-6200. Scanning electron microscope images have been obtained using MIRA3 Tescan. The roughness of the ZnO nanofilm was measured using a
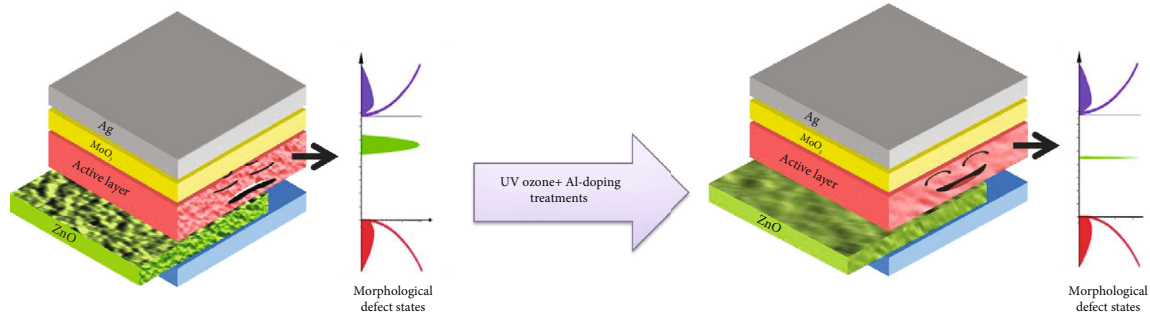
FIGURE 1: The schematic illustration of this work.

Nanosurf Mobile S atomic force microscopy instrument by WSxM software [66]. The crystalline structure of the ZnO layer was measured using XRD Tongda TD-3700. We performed impedance spectroscopy measurements using the Metrohm Autolab PGSTAT30 Potentiostat Galvanostat. The sheet resistance was estimated using a Lucas Signatone s-301-6 four-point probe instrument with a 1 mm distance between points. Contact angle measurement was done with Jikan CAG-20 using the ImageJ software contact angle plugin.

3. Device Simulation Methodology

The SCAPS-1D (version 3.3.07) was used to simulate the treatment effects. It is a one-dimensional solar cell simulator developed by the University of Gent, Belgium [67]. The package solves the Poisson and continuity equations by dividing the cell length into N intervals. Each interval's potential and carrier concentrations constitute the 3 N non-linear equations. The equations are solved by a finite difference method using the Gummel iteration scheme [68]. Device parameters related to different layers are summarized in Table 1, obtained from references [64, 69–71] and experimental (noted in the table) and fitting data. Also, Table S1 of the supplementary materials illustrates the front and back contact parameters. We used absorption coefficient spectra of active layers (Figure 2) achieved by other literates [64, 72]. Also, the AM1.5G 1sun spectrum was used, as depicted in Figure 2. The simulation focused on fitting the experimental J-V curves and studying the resulting changes in electrical properties of the ZnO layer and defect states at the interfaces and active layer. We introduced three types of defect states to all solar cells, including morphological defects in the active layer and interfacial defects in the ZnO/active layer and MoO_3/active layer interfaces. The MoO_3/active layer interfacial defects are considered less significant, because the density of generated electron-hole pairs in the ETL layer is larger than the MoO_3 layer interface due to illuminating light through the ZnO layer [73]. Also, the MoO_3 layer interface remains unaffected by the Al doping of ZnO. We modeled the distribution of defects in the active layer and the ZnO/active layer interface using the Gaussian function (gauβ). The software represents the Gaussian distribution equation according to the following:

$$N_t(E) = N_{peak} \times \exp\left[-\left(\frac{E - Et}{Ec}\right)^2\right], \text{Range}$$
$$: \left[Et - \frac{W_G}{2}Ec, Et + \frac{W_G}{2}Ec\right]. \quad (1)$$

$N_t(E)$ is the defect density with the unit of cm^{-3}/eV, and W_G is the width parameter defined to be three in this simulation. The Et and Ec are the trap level and the characteristic energy of the defect, calculated from the simulation.

The radiative recombination coefficient values for P3HT:PCBM were defined to be $5E - 15\,cm^3/s$ [71]. The nonfullerene solar cells exhibit a lower recombination rate when compared to solar cells based on fullerene [74, 75]. Therefore, the radiative recombination coefficient value for the J71:m-ITIC solar cell is defined to be zero. We also added the tail defect states to the near HOMO and LUMO levels of P3HT:PCBM [71] with electron and hole capture cross section of $1E - 18\,cm^2$, characteristic energy of 0.04 eV, and total defect density of $1E + 14\,cm^{-2}$.

4. Results and Discussion

Figure 3 (a) shows the schematic structure of the fabricated solar cell in this study. An inverted architecture was applied by employing ZnO and MoO_3 as carrier transport layers with ITO and Silver as electrodes. The study used P3HT:PCBM and J71:m-ITIC as active layer materials. Figures 3(b) and 3(c) display the SEM cross-section images of both solar cells. From the figure, the calculated thickness of the ZnO Layer for both solar cells is approximately 50 nm. Also, the thickness of the active layer for the J71:m-ITIC and P3HT:PCBM blends is 205 nm and 86 nm, respectively. Studying the morphological modifications was successfully performed using AFM and SEM images. Figure 4 shows the SEM and AFM images of ZnO layers doped with different $Al(NO_3)_3$ to ZnAc weight ratios. The root means square roughness was 1.06, 0.96, 0.99, and 1.18 nm for 0, 2, 3, and 4 wt% samples, respectively. Therefore, introducing 2 wt% $Al(NO_3)_3$ to the ZnO sample formed a relatively smooth and uniform surface compared to other Al dosages. It also can be approved by top view SEM images that the size of pinholes and cracks in 2 wt% samples is smaller than the others. Also, the ZnO thin film with 2 wt% had the smallest

TABLE 1: Material parameters used for simulation.

| Material properties	ZnO: 0 wt% Al doping	ZnO: 2 wt% Al doping	ZnO: 3 wt% Al doping	ZnO: 4 wt% Al doping	MoO$_3$	P3HT:PCBM	J71:m-ITIC
Thickness (nm)	50 (exp.)	50 (exp.)	50 (exp.)	50 (exp.)	15 (exp.)	84 (exp.)	220 (exp.)
Band gap (eV)	3.332 (exp.)	3.429 (exp.)	3.458 (exp.)	3.5 (exp.)	3 [70]	1.1 [69]	1.55 [64]
Electron affinity (eV)	4.029 [70]	3.99	3.983	3.95	2	3.65	3.05 [64]
Dielectric permittivity	9 [70]	9 [70]	9 [70]	9 [70]	35 [70]	3.8 [69]	8
CB effective DOS (1/cm^3)	$3.040E+17$	$6.040E+18$	$2.52E+19$	$5.5E+19$	$2.42E+19$ [70]	$1E+18$	$1E+18$
VB effective DOS (1/cm^3)	$4.576E+19$	$4.476E+19$	$4.476E+19$	$4.476E+19$	$2.42E+19$ [70]	$1E+19$	$1E+18$
Electron mobility (cm^2/Vs)	$7.9E+1$	$8.5E+1$	$1.29E+2$	$1.275E+2$	$5E+1$ [70]	$2.314E-4$	$5.2E-5$
Hole mobility (cm^2/Vs)	$6.1E+1$	$7E+1$	$9E+1$	$6.725E+1$	$5E+1$ [70]	$1.192E-5$	$3.5E-4$
Donor density (N_D) (cm^{-3})	$1.25E+13$	$1.3E+17$	$9.5E+17$	$5E+18$	0 [70]	0	$1E+17$
Acceptor density (N_A) (cm^{-3})	0	0	0	0	$1E+18$ [70]	$1E+15$	0
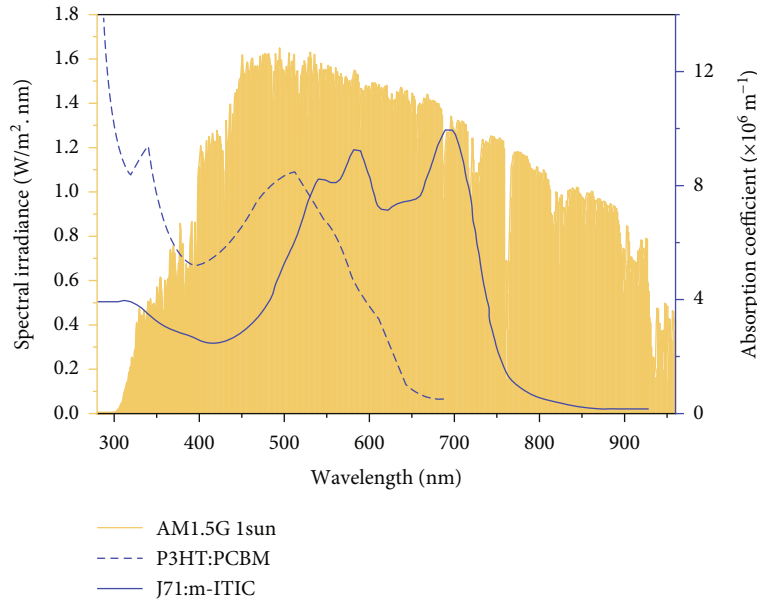
FIGURE 2: The spectrum of solar radiation AM1.5G and the absorption spectra of the P3HT:PCBM and J71:m-ITIC absorbers.

nanoparticle size among all alternative Al dosages. The average diameter of nanoparticles appears to be about 21.7, 15.4, 18.67, and 19.4 nm for 0, 2, 3, and 4 wt% samples, respectively.

X-ray diffraction measurements are applied to study the crystallization characteristics of Al-doped ZnO thin films. Figure 5(a) shows the XRD spectra of ZnO samples with 2θ ranging from 29 to 37 degrees. The ZnO sample was deposited on the ITO substrate to investigate the effect of substrate nucleation on ZnO crystallization and study the equal condition as the solar cell device prepared. The ZnO samples show a diffraction peak at about 31 degrees, which refers to the (222) crystal plane. Another diffraction peak at 35 degrees refers to the (400) plane of the ITO substrate (In$_2$O$_3$ JCPDS 06-0416) and the (002) crystal plane of ZnO (wurtzite JCPDS 036-1451). This peak shifted slightly to higher angles by increasing the Al dopant due to the difference between the ionic radius of Al and Zn atoms [76, 77], which causes compression strain on the principal axes of

the ZnO structure (a and c axes in the wurtzite structure) [78]. Figure 5(b) displays the crystallite size of the samples, calculated using the Scherrer method [79, 80]. Adding 2 wt% Al dopant has significantly decreased the crystallite size from 18.6 to 14 nm compared to bare ZnO nanofilm. However, further increase of Al dopant increased the crystallite. The calculated lattice strains for 0 wt%, 2 wt%, 3 wt%, and 4 wt% are as follows: 1.803, 0.578, 0.435, and 0.437, respectively. The average lattice strain decreased by increasing the dopant dosage. The other parameters related to XRD peaks, including d-spacing and FWHM, are given in Table S2 of the supplementary materials.

We used a four-point probe measurement to investigate the electrical properties of ZnO nanofilms. Table S3 of the supplementary materials shows the sheet resistance of ZnO samples on an ITO substrate. The calculated sheet resistance of the ZnO substrates with 0 wt%, 2 wt%, 3 wt%, and 4 wt% of Al doping is about 187.834, 165.889, 160.098, and
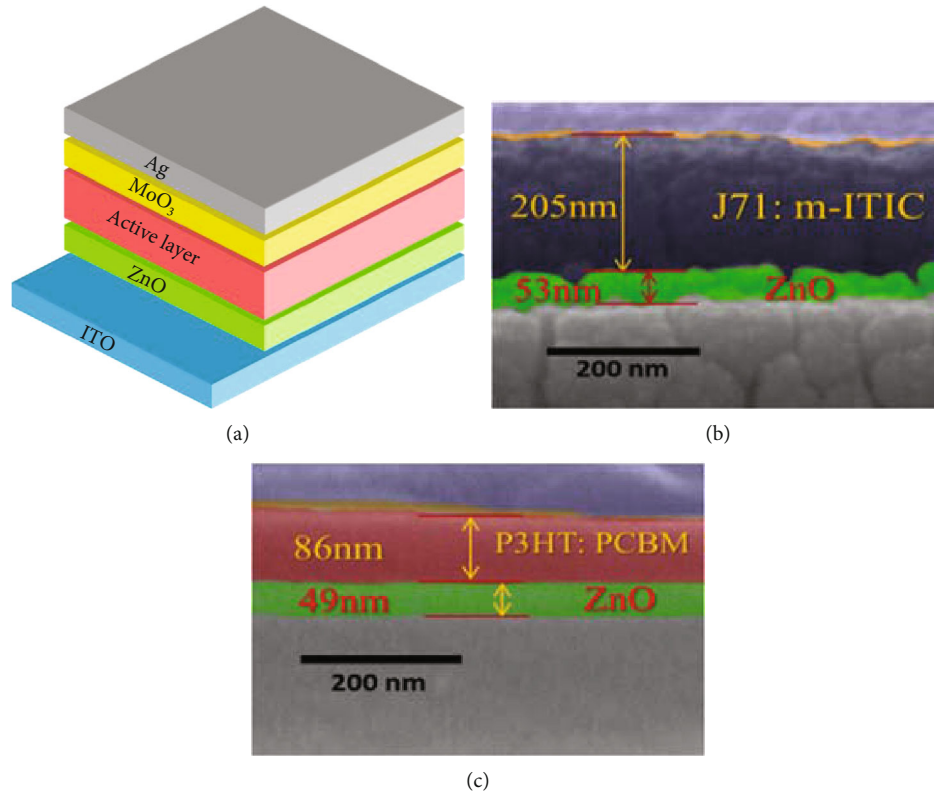
(a)

(b)

(c)

FIGURE 3: (a) The schematic device structure of the inverted organic solar cell. SEM cross-section images of (b) J71:m-ITIC and (c) P3HT:PCBM inverted solar cells.
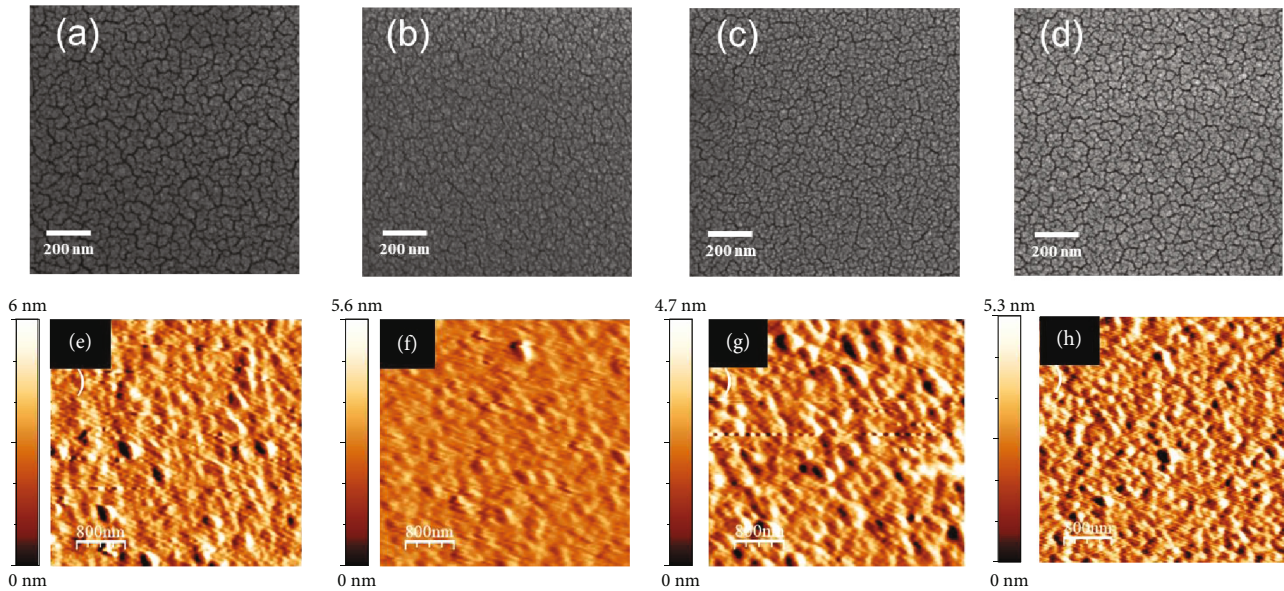

FIGURE 4: The SEM images of ZnO nanofilm with Al-doping ratio of (a) 0 wt%, (b) 2 wt%, (c) 3 wt%, and (d) 4 wt%. And AFM images of ZnO nanofilm with Al-doping ratio of (e) 0 wt%, (f) 2 wt%, (g) 3 wt%, and (h) 4 wt%.

186.099 Ω. $\square^{-1}$, respectively. The minimum value of sheet resistance was obtained for 3 wt% Al-doped ZnO thin film.

We use steady-state PL spectroscopy and UV-Vis transmittance spectroscopy to characterize the optoelectronic properties of modified ZnO layers. Zinc oxide thin films display two primary peaks corresponding to near band edge emission (NBE) and deep-level emission (DLE) trap-assisted emission [81–83]. Figure 6 shows that the PL peaks exist at 370 and 450 nm. The peak at 370 nm is associated with the PL emission of the quartz substrate, which is
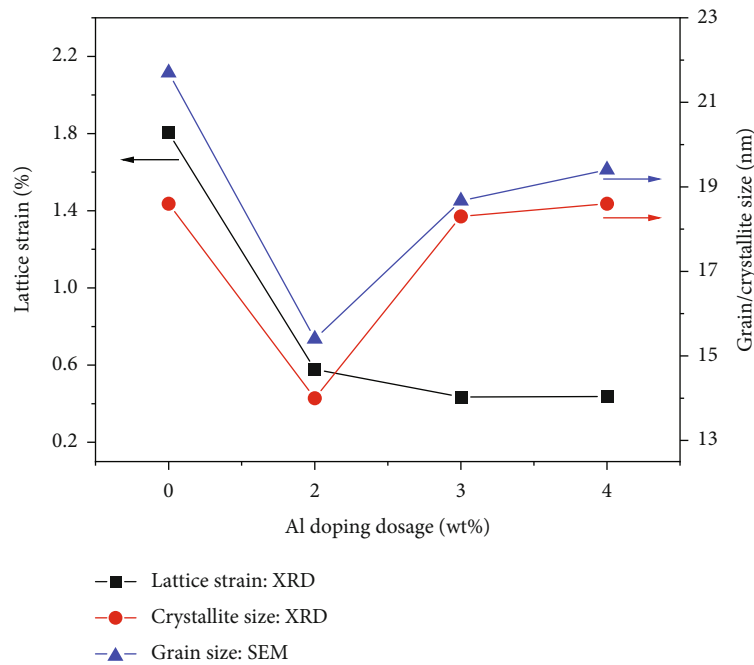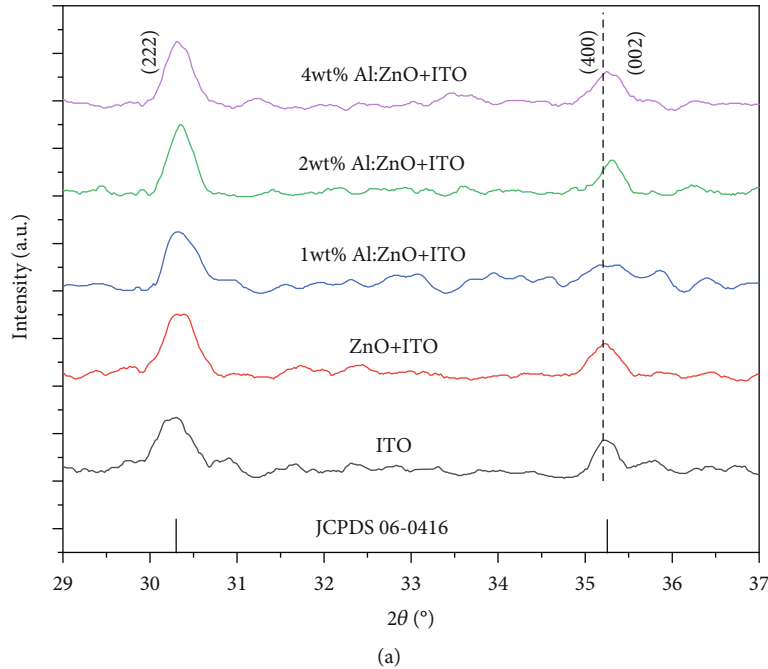
(a)

(b)

Figure 5: (a) Selected diffraction peaks of the X-ray diffraction pattern and (b) geometric parameters of ZnO nanofilms with different Al-doping ratios deposited on ITO substrate.

unreliable for monitoring the change process. However, the second peak around 450 nm related to oxygen vacancy and zinc vacancy emissions [34] shows a significant difference by changing the UV-ozone treatment time. Also, the intensity of PL peaks could give a better understanding of crystalline quality [84]. However, the measurement only focused on the wavelength shift. Applying 20 s of UV-ozone neutralized PL peaks related to oxygen vacancies (Figure 6(a)). Also, the number of peaks in this region decreased, helping

the better observation of a single peak at 468 nm (blue line). However, by extending the exposure time to 30 s, the neutralized peaks were observed again due to the formation of interstitial oxygen defects [41].

Figure 6(b) shows the PL spectra of the Al-doped ZnO layer with different doping weight percentages. A blue shift was observed for the peak at 450 nm by increasing the dopant dosage. It can be related to band edge defects passivation and the overall band gap increase while increasing the Al-
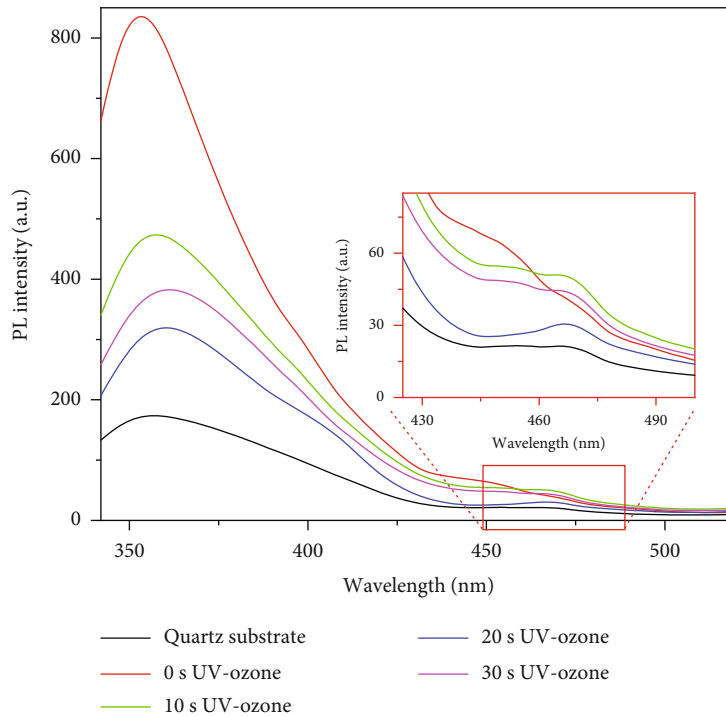
(a)
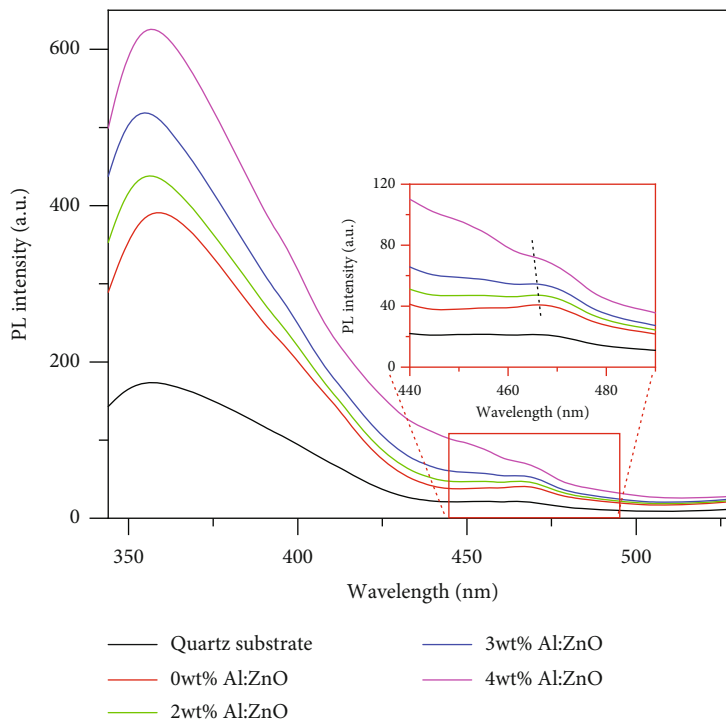
(b)

Figure 6: The photoluminescence spectra of ZnO nanofilms on quartz substrates with (a) different UV-ozone treatment times and (b) different Al-doping weight percent at 20 s of UV-ozone treatment (insets: the photoluminescence spectra focusing on a smaller wavelength range).

doping percent. For further investigation, we calculated the optical band gap of different ZnO layers using the Tauc method [85] (Figure 7). The transmittance spectra of ZnO samples indicated significant UV absorption and superior transparency in the visible region with an average of 80% transmittance. Also, from the inset of Figure 7(a), the band gap of ZnO layers was calculated to be 3.358, 3.345, 3.328, and 3.335 eV for 0 10, 20, and 30 s of UV-ozone treatment,
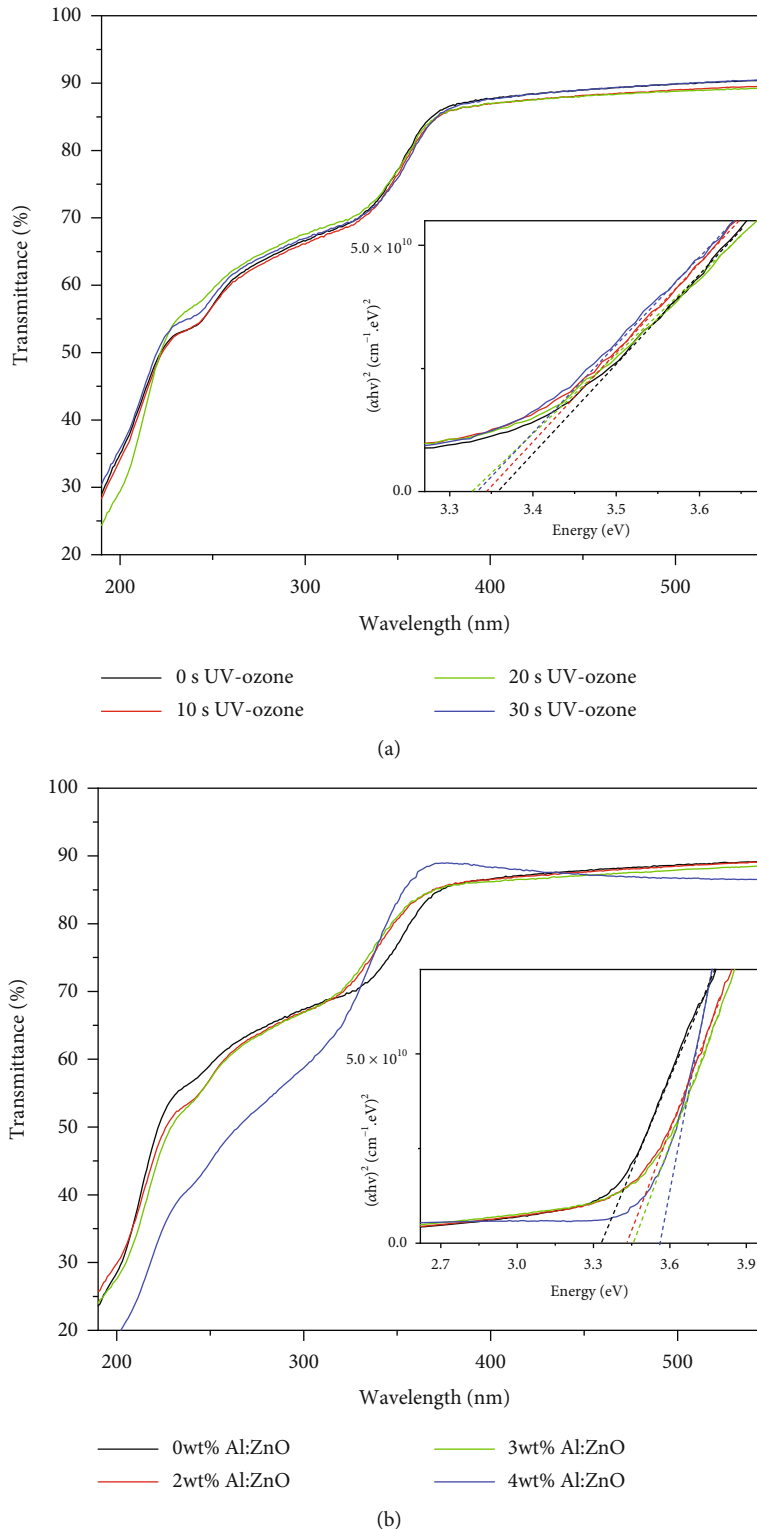
FIGURE 7: The UV-Vis absorption spectra of ZnO nanofilms on quartz substrates with (a) different UV-ozone treatment times and (b) different Al-doping weight percent at 20 s UV-ozone treatment (insets: calculated band gap using the Tauc relation).

respectively. The band gap decreased by increasing UV-Ozone treatment time. However, more than 20 s of exposure increased the band gap of ZnO samples. It may be due to neutralizing the oxygen vacancy shallow defects until 20 s and creating defects again after the 20 s UV-ozone treat-

ment, as previously discussed in the PL results. The inset of Figure 7(b) demonstrated that the band gap of Al-doped ZnO thin films is 3.332, 3.429, 3.458, and 3.562 eV for 0 wt%, 2 wt%, 3 wt%, and 4 wt%, respectively. The band gap increased by increasing dopant dosage, which is related to
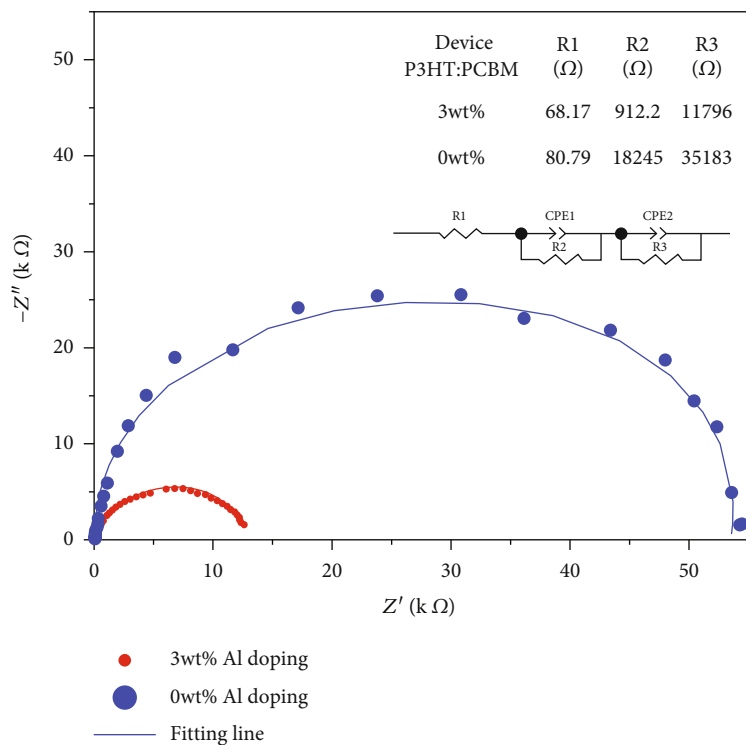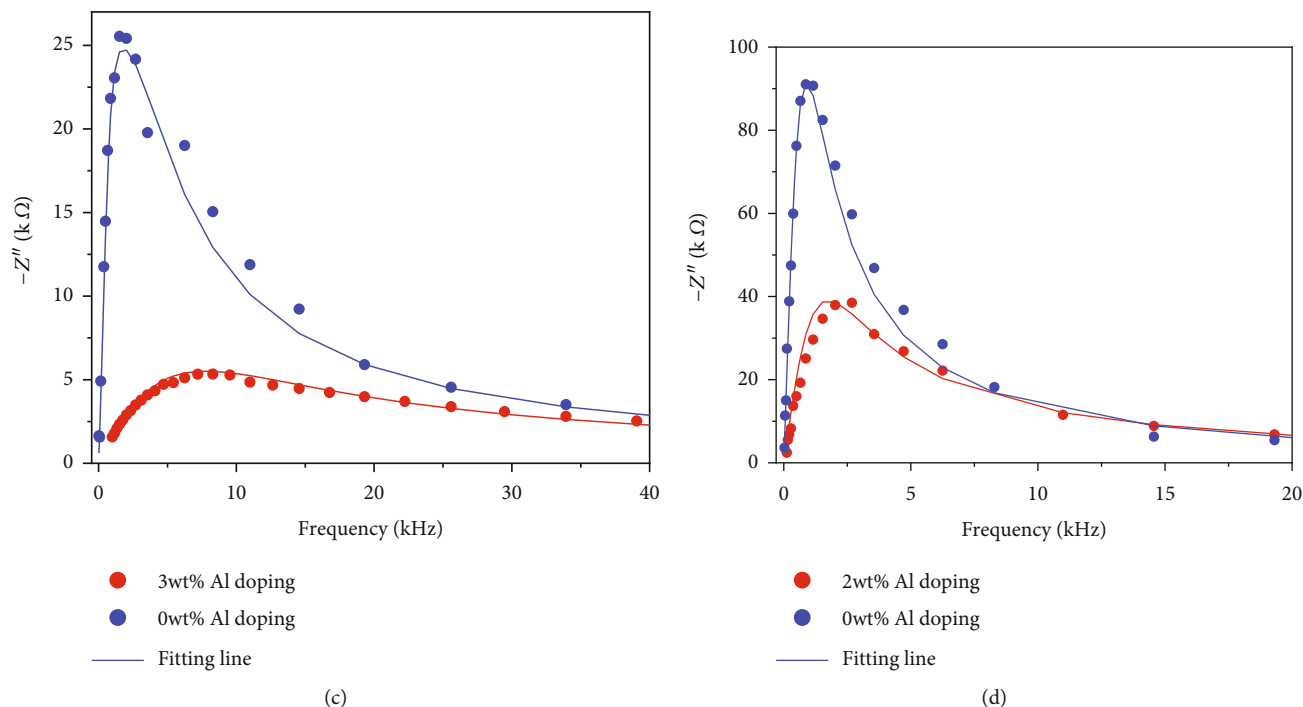
(a)
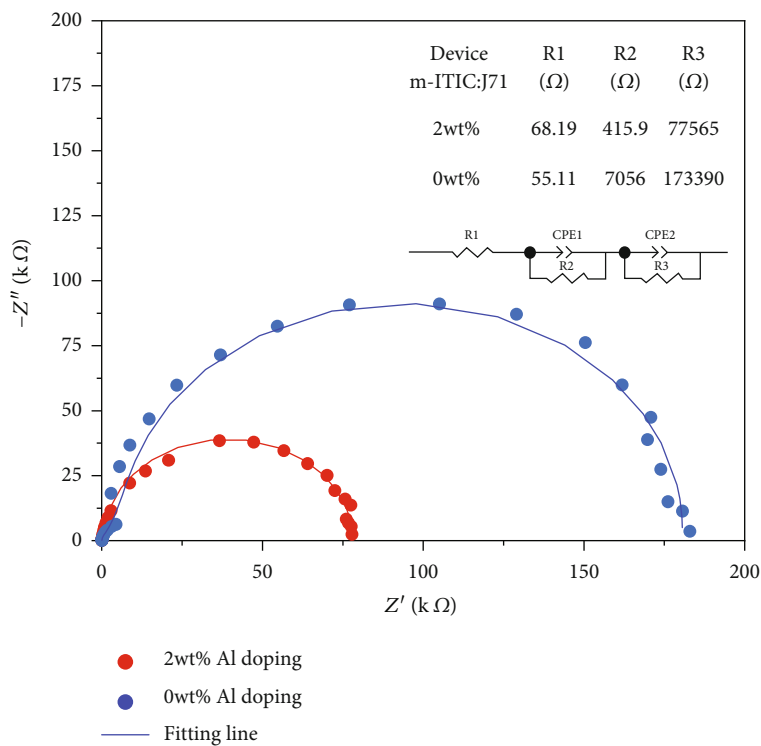
(b)

FIGURE 8: Continued.

FIGURE 8: The Nyquist plot of (a) P3HT:PCBM and (b) J71:m-ITIC solar cell (the cell area is 0.04 cm^2 for both solar cells). Insets: equivalent circuit and table of parameters. And the imaginary impedance vs. frequency of (c) P3HT:PCBM and (d) J71:m-ITIC solar cell device, with and without Al doping of the ZnO layer in optimal condition.

lattice strain changes, illustrated in Figure 5(b). In an imperfect crystal, lattice strain is proportional to lattice constant distribution [86]. By decreasing lattice strain, the average lattice constant decreases. As a result, the electrons bound more tightly to atoms, requiring more energy to excite them. Therefore, it leads to an increase in the band gap.

The impedance spectroscopy is performed in the dark using open circuit voltage bias with a frequency range of 1 kHz to 1 Hz. Figure 8 shows the Nyquist plot and the equivalent circuit for both fabricated solar cells. In the case of fitting the impedance spectra, because of unsmooth semi-circular arcs, more than one pair of parallel resistor capacitors was used in an equivalent circuit [87–89]. The R1, R2, and R3 are the parameters extracted from the fitting curve, representing series, charge transfer, and charge recombination resistance, respectively. The devices with and without Al doping show comparable values for R1. However, the device with Al-doped ZnO showed lower R2 and R3 than the ZnO samples. So, these results support the statement that Al doping helps faster electron transfer (low R2) and lower charge recombination rate (low R3) at the interface [90, 91]. Also, the frequency peak in Figures 8(c) and 8(d) shifted toward the higher frequencies by Al doping of the ZnO, indicating that Al doping decreases the relaxation time, helping better exciton dissociation and better charge transfer [92, 93]. These results are in good validation with dark J-V logarithmic curves of solar cells (Figure 9), which states that solar cells with enhancement on the ZnO layer exhibit a minor leakage current density. Therefore, Al doping reduces the shunting pathways by passivating the surface defect and shrinking pinholes.

To study the effect of UV-ozone treatment on the surface of the ZnO layer, we applied contact angle analysis immediately after UV-ozone exposure. Figure 10 shows that by increasing the UV-ozone treatment time to 20 s, the contact angle increased from 36.7° to 46.2°. However, for 30 s of UV-ozone, the contact angle decreases to 43.4°. The initial UV-ozone exposure passivates the oxygen vacancies by creating low-energy bonds. As a result, the low energy bonds reduce the hydrophilicity of the ZnO surface and increase the contact angle. Nevertheless, more reactions of ozone molecules with the surface of the ZnO layer subsequently lead to the formation of high bonding energy functional groups like hydroxyl [94, 95]. The functional groups having high energy bonds increase the surface energy and recover the hydrophilicity of the ZnO surface, leading to the decreasing contact angle [96].

Figure 11(a) shows the current-voltage (J-V) curves of fabricated J71:m-ITIC inverted solar cells and fitting curves obtained from the simulation. The average PCE for the best performing J71:m-ITIC solar cell is about 9.47%, achieved through applying 20 s of the UV-ozone treatment and 2 wt% Al doping of the ZnO layer. Figure 11(c) displays the J-V and corresponding fitting curves for P3HT:PCBM solar cells. The best-performing cell of the P3HT:PCBM solar cell showed an average PCE of 2.3% for 20 s UV-ozone treatment and 3 wt% of Al doping. The 2 wt% Al-doping samples are related to the minimum particle diameter and minimum RMS roughness of ZnO samples.

Changes in RMS roughness and particle diameter can interpret the performance of the solar cells in J-V curves. Accordingly, as the RMS roughness decreased by increasing
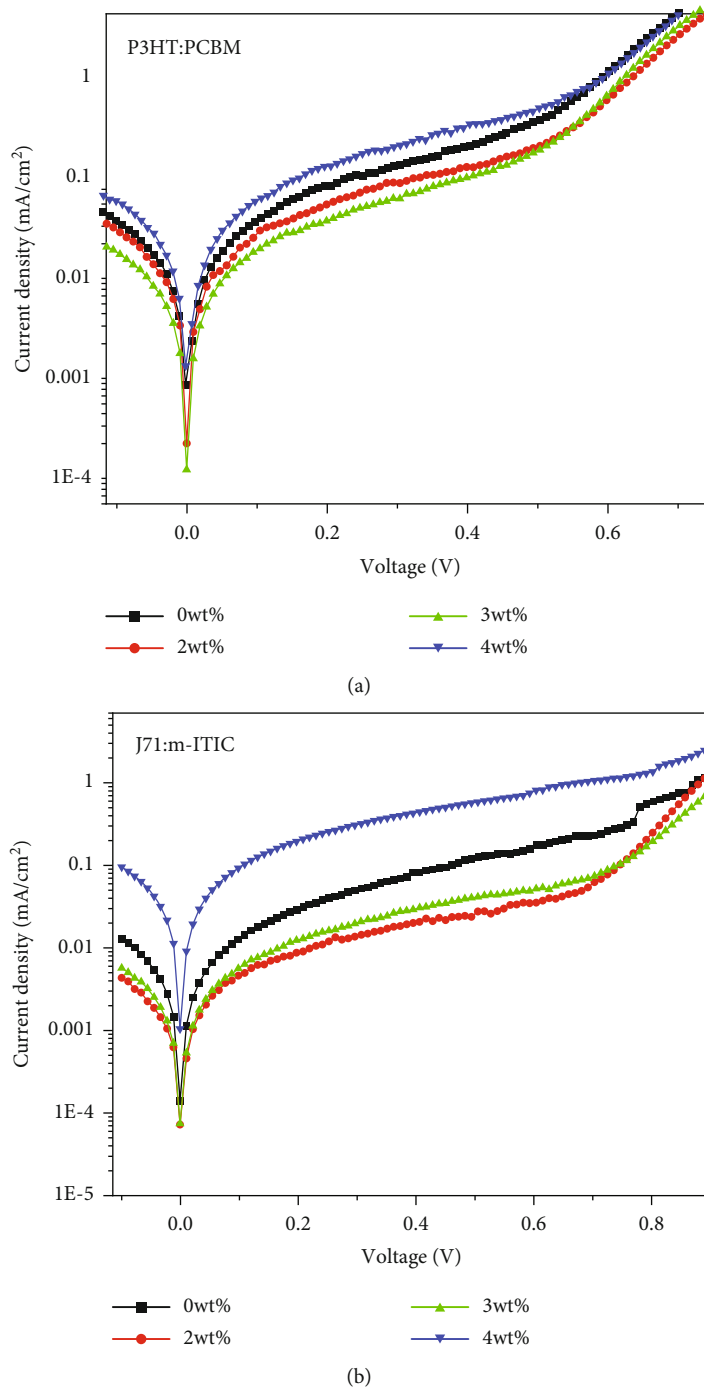
(a)

(b)

Figure 9: Dark current density-voltage curves of (a) P3HT:PCBM and (b) J71:m-ITIC solar cell with different Al-doping ratios.
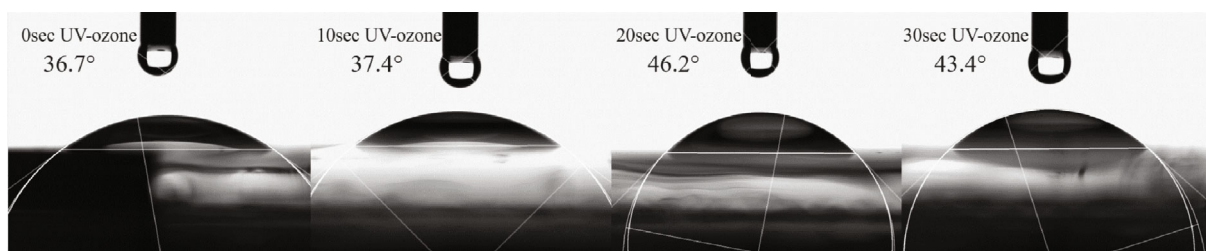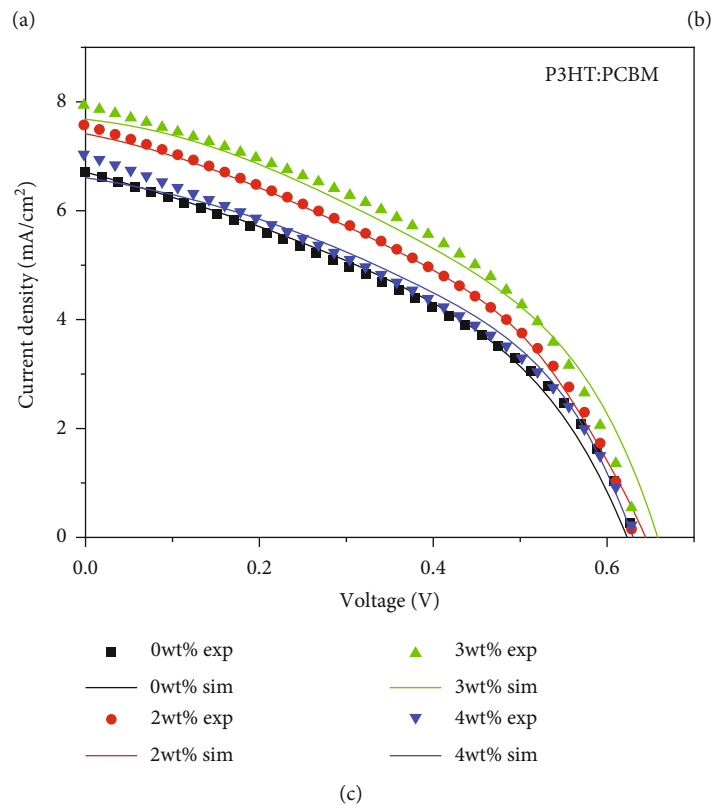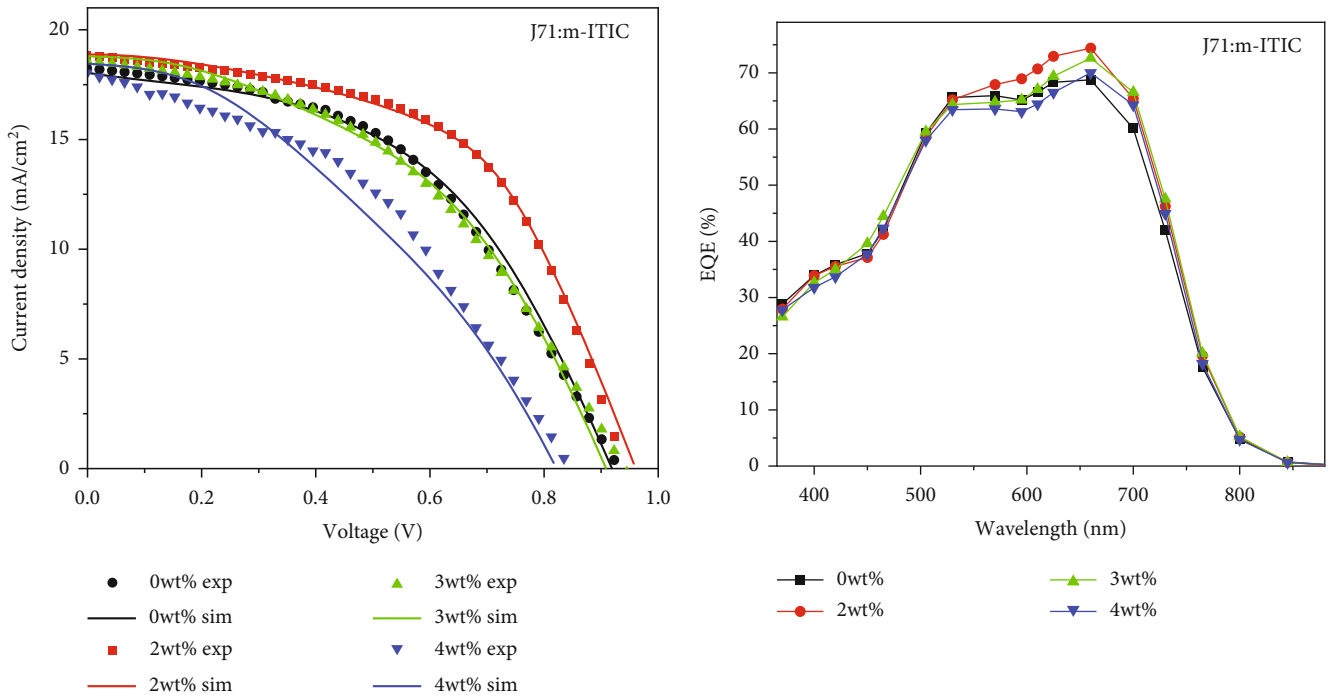

Figure 10: Contact angle measurement of ZnO nanofilms.
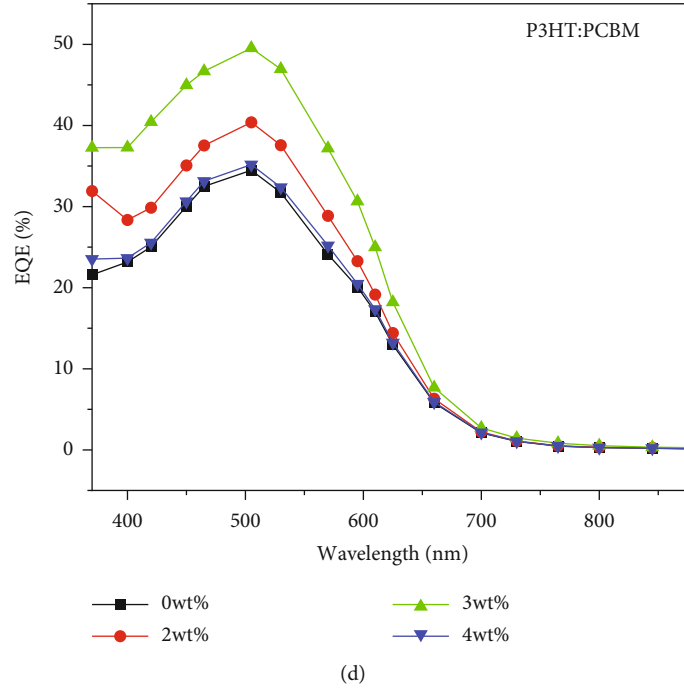
(a)

(b)

(c)

FIGURE 11: Continued.

(d)

FIGURE 11: The J71:m-ITIC solar cells: (a) current density-voltage curves of experimental and simulation fitting results and (b) related experimental EQE curves. The P3HT:PCBM solar cells: (c) current density-voltage curves of experimental and simulation fitting results and (d) related experimental EQE curves.

TABLE 2: The average photovoltaic parameters of the P3HT:PCBM and J71:m-ITIC inverted solar cells.

Active layer	UV-ozone (s)	Al doping (wt.%)	Avg. J_{sc} (mA.Cm^{-2})	Avg. V_{oc} (mV)	Avg. FF (%)	Avg. PCE (%)
P3HT:PCBM	0	0%	6.30	642.0	40.0	1.67
		3%	7.46	644.8	39.7	1.85
	20	0%	7.27	634.5	40.3	1.83
		3%	8.26	644.7	40.7	2.32
J71:m-ITIC	0	0%	16.38	830.9	40.3	5.48
		2%	18.02	850.9	41.8	6.41
	20	0%	17.89	932.2	49.1	8.17
		2%	19.11	935.2	53.1	9.47

the dopant dosage from 1 wt% to 2 wt%, the FF and J_{sc} of J71:m-ITIC were significantly improved. Further increase in dopant dosage led to a decrease in FF and J_{sc}. Thus, for the cell with 4 wt% of Al doping, which has the highest RMS roughness and a particle diameter close to blank samples, the FF and J_{sc} of solar cells were drastically decreased. The process of changes is not the same for P3HT:PCBM system. For P3HT:PCBM solar cells, by increasing dopant dosage, the J_{sc} of the cell showed significant change, while other parameters illustrated minor differences. At 3 wt% of Al doping, which is not the sample with the lowest RMS roughness and particle diameter, the highest value for J_{sc} was achieved. The notable feature of 3 wt% compared to others is the low sheet resistance. It can be concluded that the P3HT:PCBM system is mainly affected by the sheet resistivity of ZnO layers rather than the RMS roughness and particle size. For 4 wt% of the P3HT:PCBM solar cell,

the performance parameters returned to the none-doping sample parameters because of increasing both RMS roughness and sheet resistance of the ZnO layer.

The average performance characteristics of all solar cells, including open circuit voltage (V_{oc}), short circuit current density (J_{sc}), and filling factor (FF), are indicated in Table 2. From the table, the Al doping extensively affects the J_{sc} of the P3HT:PCBM solar cell due to improving the conductivity of the ZnO layer. Also, the maximum J_{sc} for J71:m-ITIC solar cell was achieved for the sample with the lowest RMS roughness and particle diameter (2 wt%), which indicates that in addition to sheet resistance, the interfacial defects derived from morphological disorders of the ZnO layer influenced the current density of charge carriers.

Moreover, the V_{oc} of both solar cells showed a slight improvement for the smoother surface morphology of the Al-doped ZnO due to the reduced recombination rate at
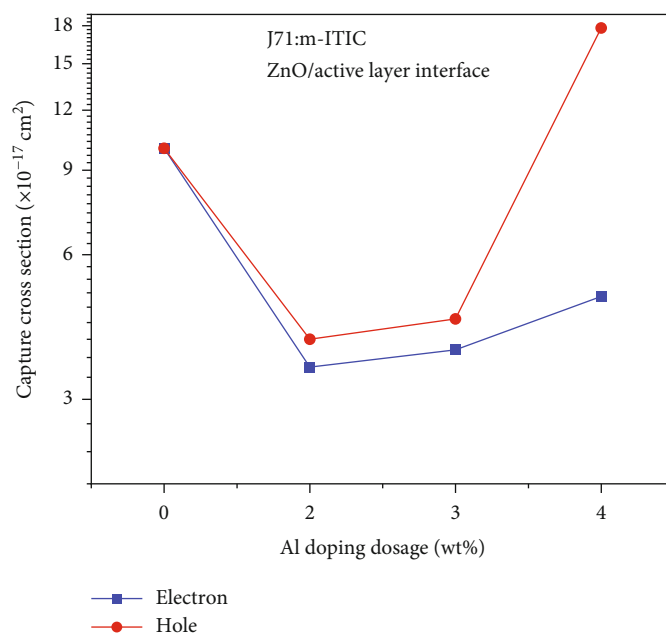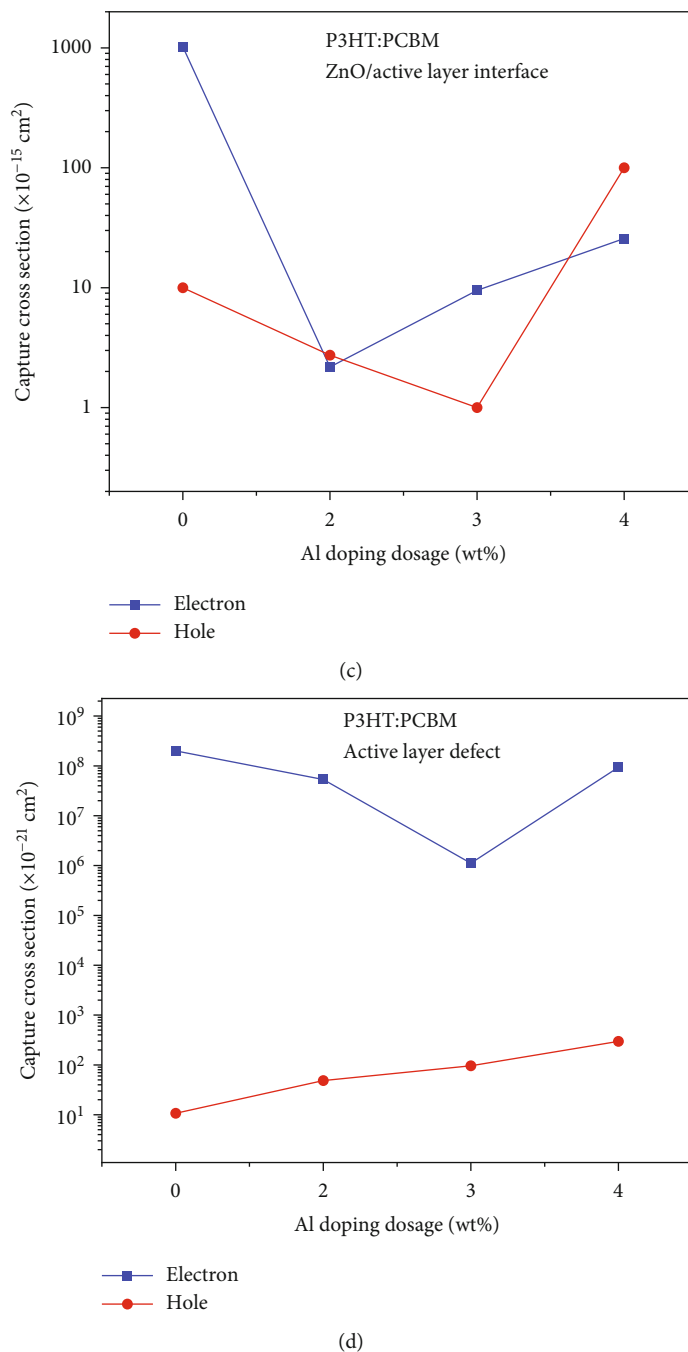
(a)
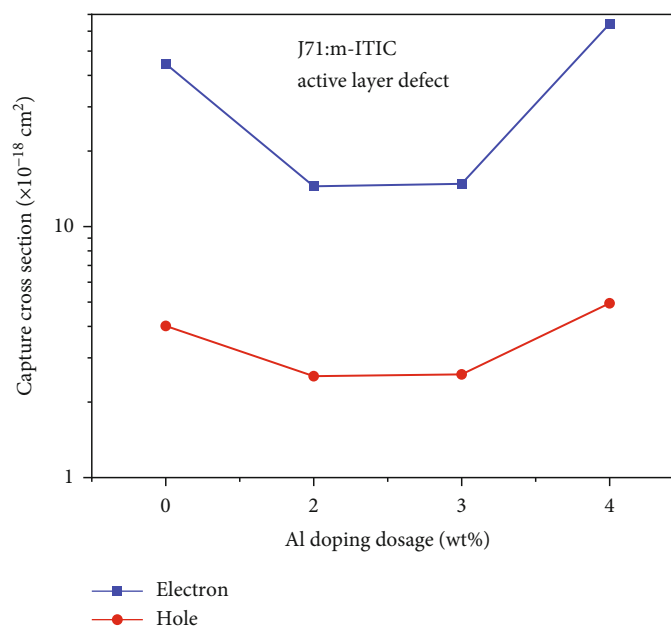
(b)

FIGURE 12: Continued.

(c)

(d)

FIGURE 12: The electron and hole capture cross sections of J71:m-ITIC solar cell at (a) ZnO/J71:m-ITIC active layer interface, (b) inside J71:m-ITIC active layer, (c) ZnO/P3HT:PCBM active layer interface, and (d) inside P3HT:PCBM active layer for different Al dopants of ZnO.

the ZnO/active layer interface. The impact of interfacial defects is investigated further in the simulation results. Also, a few increases in built-in potential by changing the work function of the ZnO layer may affect the V_{oc} of the J71:m-ITIC solar cell [97]. The FF of P3HT:PCBM solar cell did not show a noticeable change by Al doping. However, for the J71:m-ITIC solar cell, the FF was improved by Al doping of the ZnO layer. Because in the J71:m-ITIC solar cell, the interfacial defects and the morphology of the active layer are strongly dependent on the surface roughness of the ZnO layer. This proposed reason was also investigated in

the theoretical part. The UV-ozone treatment enhanced the J_{sc} of the P3HT:PCBM solar cell due to reducing the ZnO/active layer interfacial defects by passivating the oxygen vacancies. Also, for the J71:m-ITIC solar cell, the UV-ozone treatment improved the J_{sc}, V_{oc}, and FF, indicating that interfacial effects significantly impact the J71:m-ITIC solar cells. Using UV-ozone, the current density, which is directly affected by interface traps, was increased. The increase of J_{sc}, V_{oc}, and FF is also due to decreasing the interfacial traps, reducing the recombination rate, and lowering current leakage at the interface.
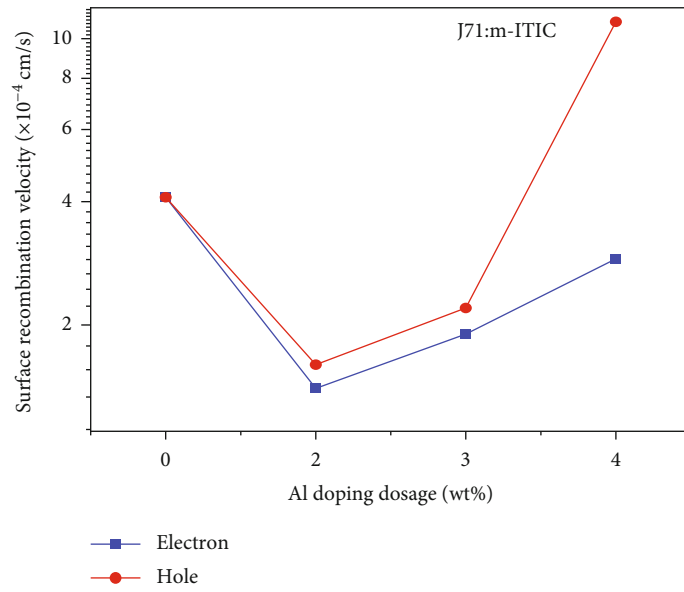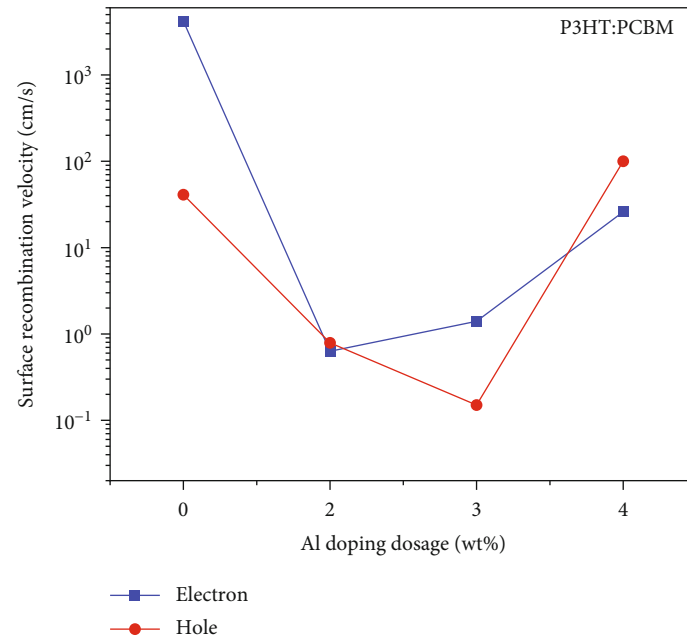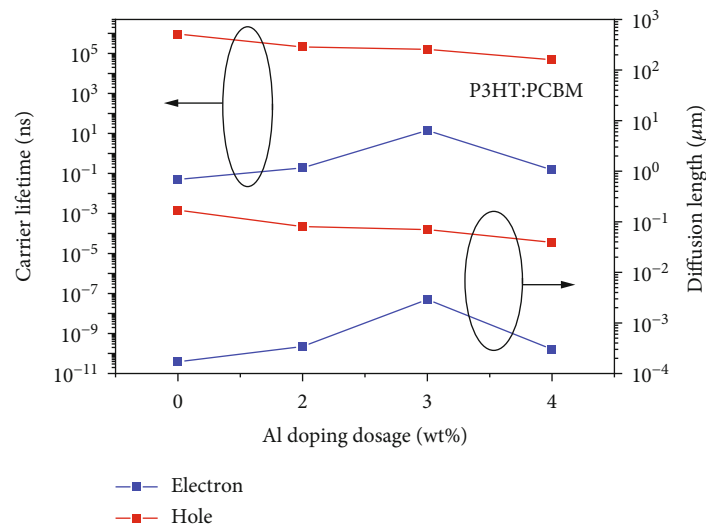
(a)
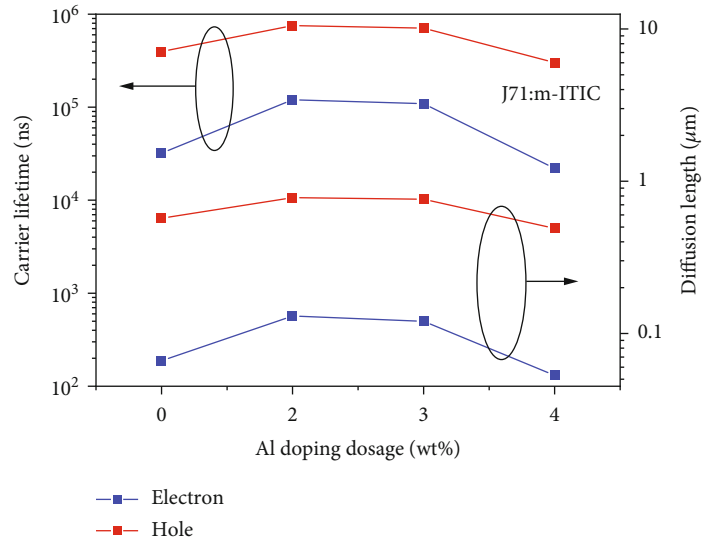
(b)

FIGURE 13: Continued.

(c)

(d)

FIGURE 13: (a) Surface recombination velocity at the ZnO/J71:m-ITIC active layer interface, (b) the carrier lifetime and diffusion length of the J71:m-ITIC active layer, (c) surface recombination velocity at ZnO/P3HT:PCBM active layer interface for different Al dopants of ZnO, and (d) carrier lifetime and diffusion length of the P3HT:PCBM active layer.

The J71:m-ITIC solar cells demonstrated a J_{sc} of 19.1 mA.cm^{-2}, exceeding the previously reported value of 18.09 mA.cm^{-2} [64]. In Figure 1(b), the SEM cross-section image shows that the active layer thickness surpasses the previously reported range of 100-150 nm [98, 99]. The thicker active layer led to more absorption of photons and an increase in the photocurrent density. Figure S1 of the supplementary materials indicates the impact of the absorber layer thickness on J_{sc} and other crucial performance parameters of J71:m-ITIC solar cells achieved from simulation. From the figure, increasing the thickness of the absorber layer leads to more exciton generation, which enhances J_{sc} and PCE. However, more enlargements

in thickness hinder significant increment in J_{sc} due to increasing the recombination of diffused carriers. As the thickness of the absorber raised, the V_{oc} increased until it reached its maximum potential, attributed to the dark saturation current increase, resulting in improved charge carrier recombination [73]. However, the filling factor reduced as thickness increased because the series resistance of the active layer increased [100, 101].

Figures 11(b) and 11(d) show the EQE spectra of J71:m-ITIC and P3HT:PCBM solar cells, respectively. At 3 wt% of Al doping, the P3HT:PCBM device demonstrates a superior EQE than any other, while the J71:m-ITIC solar cell exhibits optimal performance with 2 wt% of Al doping.
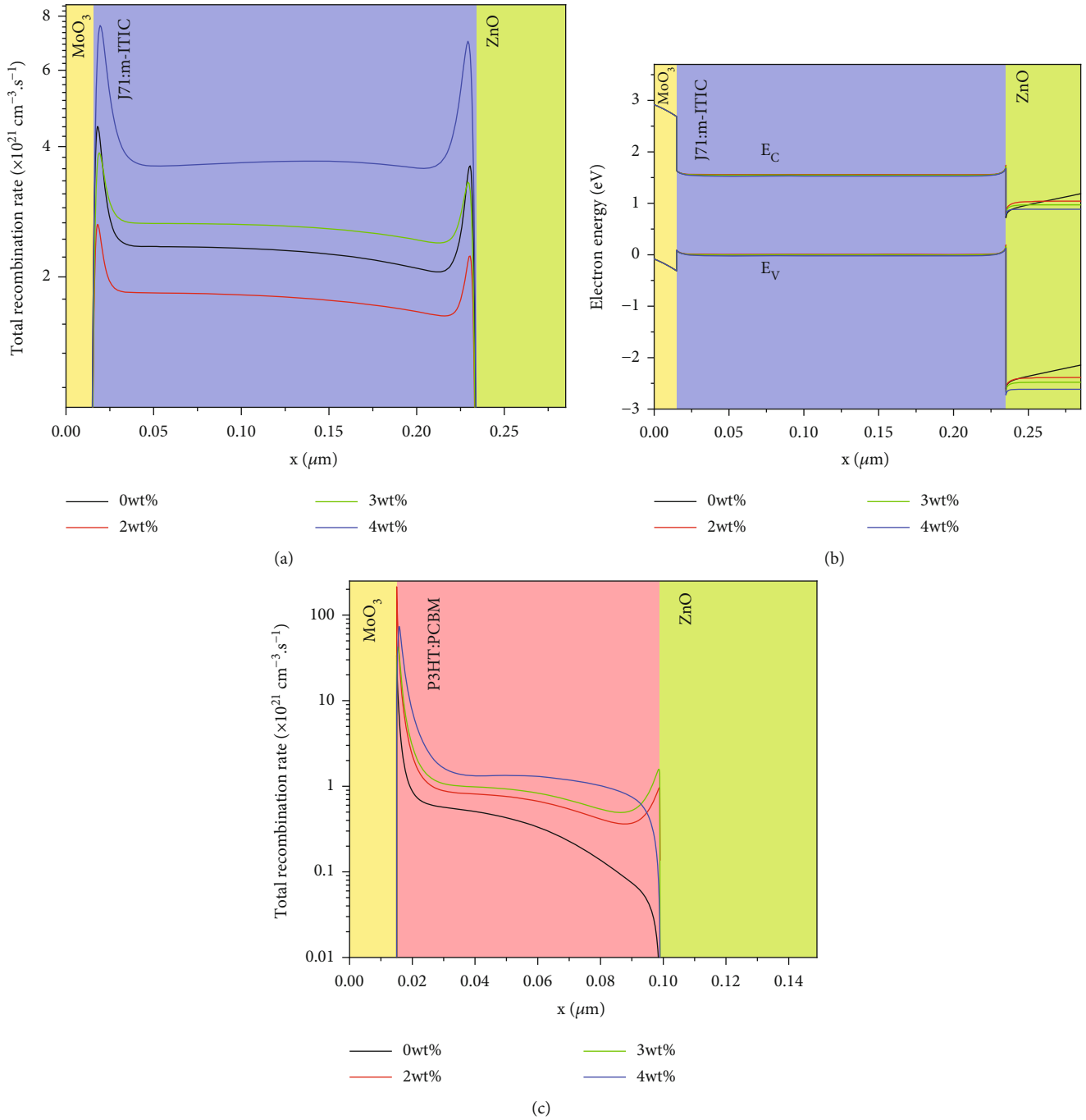
(a)
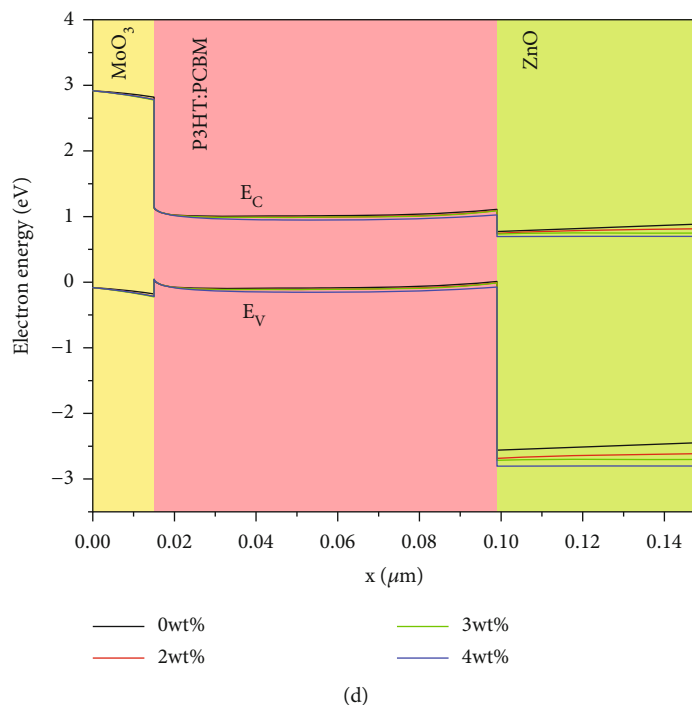

(b)

(c)

FIGURE 14: Continued.

(d)

FIGURE 14: (a) The recombination rate and (b) energy band diagram of J71:m-ITIC solar cell for different Al dopants. (c) The recombination rate and (d) energy band diagram of P3HT:PCBM solar cell for different Al dopants.

The performance parameters of the simulation results are shown in Tables S4 and S5 of supplementary materials. The PCE obtained from the simulation for best-performing J71:m-ITIC and P3HT:PCBM solar cells is about 9.78% and 2.17%, respectively, which agrees with experimental work. The carrier capture cross-section (CCS) is the first represented analytical result calculated from the simulation. Figure 12 shows the CCSs related to the defects at the ZnO/active layer interface and inside the active layer of J71:m-ITIC and P3HT:PCBM solar cells. According to the CCS curves, adding 2 wt% of Al dopant in both solar cells reduced the electron and hole CCSs at the ZnO/active layer interface. However, the CCS slightly raised by increasing the dopant dosage to 3 wt%. The CCS further increased at a dopant dosage of 4 wt%. The results indicate that carrier transport at the ZnO/active layer interface follows the same trend as RMS roughness and crack size change (AFM and SEM images in Figure 4). Figure 12(b) shows the CCS of J71:m-ITIC active layer, which follows the same pattern as the interfacial CCSs change. The ZnO layer as a bottom layer affects the morphology of the active layer and induces defects within the band gap of the organic blend. Therefore, having a smooth ZnO surface decreased the active layer trap states.

On the other hand, the CCS in the active layer of P3HT:PCBM does not follow a specific trend compared to the J71:m-ITIC solar cell, demonstrating that Al doping does not affect the traps of P3HT:PCBM layer. Figure S2 of the supplementary materials also depicts the total defect density of both solar cells, including the defects in the active layer and the ZnO/active interface.

Figure 13 illustrates the active layer carrier lifetime, diffusion length, and surface recombination velocity at the ZnO/active layer interface for both P3HT:PCBM and J71:m-ITIC solar cells. The surface recombination velocity in both devices decreased drastically in 2 wt% of Al doping. However, increasing Al doping to 3 wt% and 4 wt% increased the surface recombination velocity. Comparing surface recombination velocity curves with capture cross-section curves (Figures 12(a) and 12(c)) shows a good analogy between them. Also, the carrier lifetime and diffusion length curves are inversely related to electron and hole capture cross-section curves of both solar cells (Figures 12(b) and 12(d)). Adding 2 wt% of Al dopant increases the carrier lifetime and diffusion length inside the J71:m-ITIC active layer. However, more doping dosage decreased both carrier lifetime and diffusion length. For P3HT:PCBM solar cell, carrier lifetime and diffusion length demonstrated different behaviors for electrons and holes and did not follow a particular trend, concluding that there is no relation between the surface morphology of the ZnO layer and the active layer defects of the P3HT:PCBM solar cell.

Figure 14 shows the total recombination rate and energy band diagram of J71:m-ITIC and P3HT:PCBM solar cells at different Al dopants of the ZnO layer. At 2 wt% of Al doping, the total recombination rate of J71:m-ITIC solar cells decreased due to the reduction of CCSs at the interface and active layer. However, the total recombination rate of the P3HT:PCBM solar cell increased with decreasing CCSs. In P3HT:PCBM solar cells, low surface recombination velocities (around $1\,cm.s^{-1}$) induced a pile-up of charge carriers in the device, leading to the total recombination increase [102].
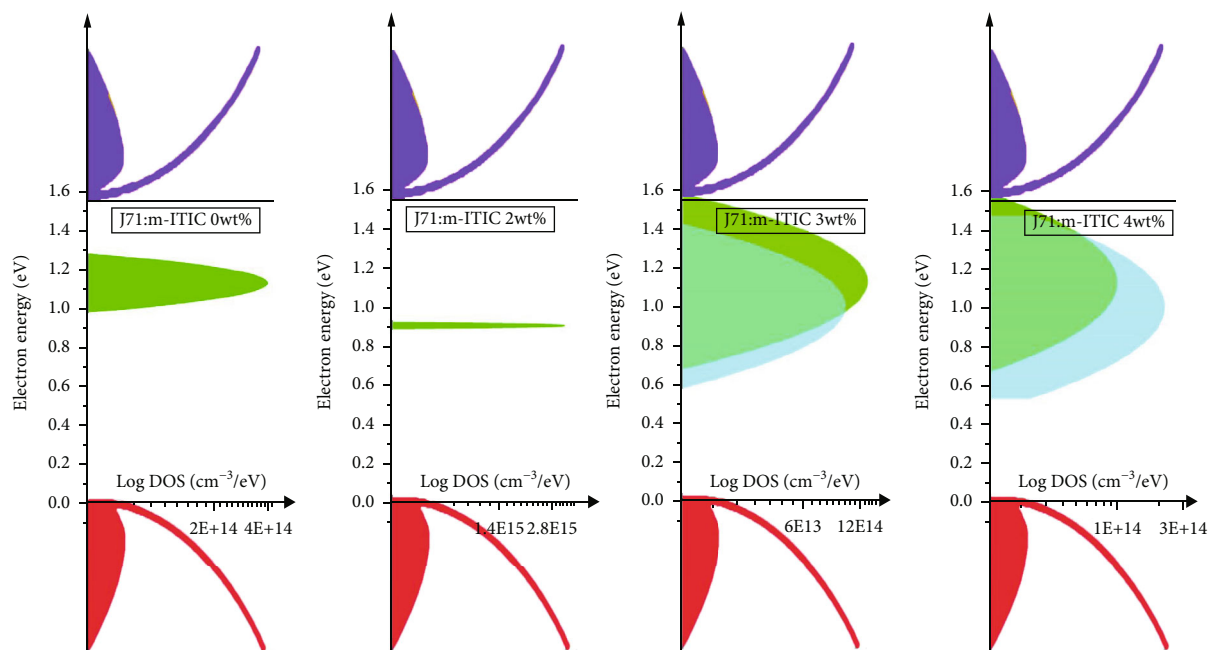
FIGURE 15: The calculated density of morphological defect states of the J71:m-ITIC active layer for different Al dopants.

Also, the energy band diagram of both samples indicates that adding Al dopant to ZnO may affect the ZnO band gap and electron affinity.

Figure 15 visualizes the morphological defect states of the J71:m-ITIC active layer for different Al dopants of ZnO. The density of the states (DOS) above LUMO and below the HOMO levels illustrates the schematic band diagram of the active layer. From the figure, the defect state width decreased by increasing the Al doping to 2 wt%. With more increase in the Al doping, the defect state width increased. However, the DOS of the P3HT:PCBM layer (Figure S3 of the supplementary materials) did not show a significant change by changing the dopant dosage of the ZnO layer. The P3HT:PCBM layer contains inherent defect states [103, 104] within the band gap, which could potentially overshadow the impacts of any new defects. Also, because of the ball-shaped structure of fullerenes, controlling the blend morphology is straightforward, and they always showed the same crystallinity and phase separation. However, non-fullerene acceptors have a planer structure, which makes phase separation difficult [56, 105]. When the substrate is not smooth enough, phase separation on an appropriate scale with the proper molecular orientation is even more problematic. Consequently, it leads to unfavorable BHJ blend morphology, high exciton recombination, and inefficient charge transfer.

5. Conclusion

UV-ozone treatment combined with Al doping for the ZnO ETL layer improved the efficiency of non-fullerene and fullerene-based solar cells. The UV-ozone treatment passivated the oxygen vacancy defect states, improving the optoelectrical properties of the ZnO layer. The 2 wt% Al-doped ZnO reduced pinholes and surface roughness, while the resistance decreased to a minimum for 3 wt% of Al doping. From simulation results, adding 2 wt% of Al decreased the surface recombination velocity at the ZnO/active layer interface. The carrier lifetime and diffusion length of the J71:m-ITIC layer increased with 2 wt% of Al doping. The morphological defect state of the P3HT:PCBM layer is not much affected by the Al doping due to the overshadowing effect of intrinsic traps. Therefore, the P3HT:PCBM solar cell exhibited the highest efficiency at 3 wt% Al doping, while the J71:m-ITIC solar cell showed the highest efficiency at 2 wt%. The methods are simple and have a remarkable impact on boosting performance, paving the way for organic photovoltaic mass production.

Data Availability

The datasets used and/or analysed during the current study are available from the corresponding author on reasonable request.

Conflicts of Interest

The authors declare that they have no conflicts of interest.

Acknowledgments

Western Australia, as part of the Wiley-The University of Western Australia agreement via the Council of Australian University Librarians.

Supplementary Materials

Table S1 presents the parameters used in the simulation for the solar cell device's front and back contacts. Table S2 shows the XRD average geometric parameters of ZnO nanofilms under varying Al-doping ratios which were calculated by the Scherrer method. Table S3 presents the electrical properties of ZnO thin films with different Al-doping ratios obtained by the four-point probe method. Table S4 and Table S5 display the performance parameters of the J71:m-ITIC and P3HT:PCBM solar cells, both obtained through simulation. Figure S1 depicts the impact of absorber layer thickness on the performance of the J71:m-ITIC solar cell with 2% Al-doped ZnO obtained from the simulation. Figure S2 illustrates the total defect density of J71:m-ITIC and P3HT:PCBM solar cells at the interface of the ZnO/active layer and within the active layer. Also, the simulation results in Figure S3 show the density of morphological defect states in P3HT:PCBM active layer for varying Al dopants of ZnO. *(Supplementary Materials)*

References

[1] S. Logotshetidis, "Flexible organic electronic devices: materials, process and applications," *Materials Science and Engineering B*, vol. 152, no. 1-3, pp. 96–104, 2008.

[2] T. R. Andersen, H. F. Dam, M. Hösel et al., "Scalable, ambient atmosphere roll-to-roll manufacture of encapsulated large area, flexible organic tandem solar cell modules," *Energy & Environmental Science*, vol. 7, no. 9, pp. 2925–2933, 2014.

[3] Y. Huang, E. J. Kramer, A. J. Heeger, and G. C. Bazan, "Bulk heterojunction solar cells: morphology and performance relationships," *Chemical Reviews*, vol. 114, no. 14, pp. 7006–7043, 2014.

[4] Z. Li, K. Jiang, G. Yang et al., "Donor polymer design enables efficient non-fullerene organic solar cells," *Nature Communications*, vol. 7, no. 1, article 13094, 2016.

[5] F. Zhao, J. Zhou, D. He, C. Wang, and Y. Lin, "Low-cost materials for organic solar cells," *Journal of Materials Chemistry C*, vol. 9, no. 43, pp. 15395–15406, 2021.

[6] V. S. Gevaerts, L. J. A. Koster, M. M. Wienk, and R. A. J. Janssen, "Discriminating between bilayer and bulk heterojunction polymer:fullerene solar cells using the external quantum efficiency," *ACS Applied Materials & Interfaces*, vol. 3, no. 9, pp. 3252–3255, 2011.

[7] A. Loiudice, A. Rizzo, M. Biasiucci, and G. Gigli, "Bulk heterojunction versus diffused bilayer: the role of device geometry in solution p-doped polymer-based solar cells," *Journal of Physical Chemistry Letters*, vol. 3, no. 14, pp. 1908–1915, 2012.

[8] W. Xu, M. Zhang, X. Ma et al., "Over 17.4% efficiency of layer-by-layer all-polymer solar cells by improving exciton utilization in acceptor layer," *Advanced Functional Materials*, vol. 33, no. 28, article 2215204, pp. 1–8, 2023.

[9] Y. Cui, Y. Xu, H. Yao et al., "Single-junction organic photovoltaic cell with 19% efficiency," *Advanced Materials*, vol. 33, no. 41, article e2102420, 2021.

[10] C. Xu, Z. Zhao, K. Yang et al., "Recent progress in all-small-molecule organic photovoltaics," *Journal of Materials Chemistry A*, vol. 10, no. 12, pp. 6291–6329, 2022.

[11] W. Xu, X. Ma, J. H. Son et al., "Smart ternary strategy in promoting the performance of polymer solar cells based on bulk-heterojunction or layer-by-layer structure," *Small*, vol. 18, no. 4, article 2104215, 2022.

[12] J. Tan, Y. Zhao, G. Li, S. Yang, C. Huang, and H. Yu, "High-performance organic solar cells by adding two-dimensional GeSe," *Advanced Functional Materials*, vol. 32, no. 52, article 2209094, 2022.

[13] B. Olyaeefar, A. Asgari, and S. Ahmadi-kandjani, "Effective thickness method for modeling absorption enhancement of forward-scattering nanoparticles in photovoltaic devices," *Solar Energy Materials & Solar Cells*, vol. 215, article 110688, 2020.

[14] E. A. Milani, M. Piralaee, S. Ahmadi, and A. Asgari, "The role of structural parameters on efficiency and transparency of semi-transparent non-fullerene organic solar cell," *Scientific Reports*, vol. 12, no. 1, article 14928, 2022.

[15] S. Lattante, "Electron and hole transport layers: their use in inverted bulk heterojunction polymer solar cells," *Electronics*, vol. 3, no. 1, pp. 132–164, 2014.

[16] C. Hou and H. Yu, "ZnO/Ti3C2Tx monolayer electron transport layers with enhanced conductivity for highly efficient inverted polymer solar cells," *Chemical Engineering Journal*, vol. 407, article 127192, 2021.

[17] J. Zhang, C. Huang, Y. Sun, and H. Yu, "Amino-functionalized niobium-carbide MXene serving as electron transport layer and perovskite additive for the preparation of high-performance and stable methylammonium-free perovskite solar cells," *Advanced Functional Materials*, vol. 32, no. 24, article 2113367, 2022.

[18] W. C. H. Choy and D. Zhang, "Solution-processed metal oxides as efficient carrier transport layers for organic photovoltaics," *Small*, vol. 12, no. 4, pp. 416–431, 2016.

[19] M. Li, W. Ni, B. Kan et al., "Graphene quantum dots as the hole transport layer material for high-performance organic solar cells," *Physical Chemistry Chemical Physics*, vol. 15, no. 43, pp. 18973–18978, 2013.

[20] Y. Sun, J. H. Seo, C. J. Takacs, J. Seifter, and A. J. Heeger, "Inverted polymer solar cells integrated with a low-temperature-annealed sol-gel-derived ZnO film as an electron transport layer," *Advanced Materials*, vol. 23, no. 14, pp. 1679–1683, 2011.

[21] J. Huang, Z. Yin, and Q. Zheng, "Applications of ZnO in organic and hybrid solar cells," *Energy & Environmental Science*, vol. 4, no. 10, p. 3861, 2011.

[22] T. Stubhan, H. Oh, L. Pinna, J. Krantz, I. Litzov, and C. J. Brabec, "Inverted organic solar cells using a solution processed aluminum-doped zinc oxide buffer layer," *Organic Electronics*, vol. 12, no. 9, pp. 1539–1543, 2011.

[23] C. Waldauf, M. Morana, P. Denk et al., "Highly efficient inverted organic photovoltaics using solution based titanium oxide as electron selective contact," *Applied Physics Letters*, vol. 89, no. 23, pp. 1–4, 2006.

[24] H. Schmidt, K. Zilberberg, S. Schmale, H. Flügge, T. Riedl, and W. Kowalsky, "Transient characteristics of inverted polymer solar cells using titaniumoxide interlayers," *Applied Physics Letters*, vol. 96, no. 24, article 243305, 2010.

[25] D. K. Chaudhary, P. K. Dhawan, S. P. Patel, and H. P. Bhasker, "Large area semitransparent inverted organic solar cells

with enhanced operational stability using TiO2 electron transport layer for building integrated photovoltaic devices," *Materials Letters*, vol. 283, article 128725, 2021.

[26] S. Jiang, X. Chen, Y. Bai et al., "Water-soluble SnO2nanoparticles as the electron collection layer for efficient and stable inverted organic tandem solar cells," *ACS Applied Energy Materials*, vol. 3, no. 12, pp. 12662–12671, 2020.

[27] Y. Bai, C. Zhao, X. Chen et al., "Interfacial engineering and optical coupling for multicolored semitransparent inverted organic photovoltaics with a record efficiency of over 12%," *Journal of Materials Chemistry A*, vol. 7, no. 26, pp. 15887–15894, 2019.

[28] V.-H. Tran, S. H. Eom, S. C. Yoon, S.-K. Kim, and S.-H. Lee, "Enhancing device performance of inverted organic solar cells with SnO2/Cs2CO3 as dual electron transport layers," *Organic Electronics*, vol. 68, pp. 85–95, 2019.

[29] J. You, C.-C. Chen, L. Dou et al., "Metal oxide nanoparticles as an electron-transport layer in high-performance and stable inverted polymer solar cells," *Advanced Materials*, vol. 24, no. 38, pp. 5267–5272, 2012.

[30] D. Ouyang, Z. Huang, and W. C. H. Choy, "Solution-processed metal oxide nanocrystals as carrier transport layers in organic and perovskite solar cells," *Advanced Functional Materials*, vol. 29, no. 1, article 1804660, 2019.

[31] J. You, L. Meng, T. Bin Song et al., "Improved air stability of perovskite solar cells via solution-processed metal oxide transport layers," *Nature Nanotechnology*, vol. 11, no. 1, pp. 75–81, 2016.

[32] Z. Liang, Q. Zhang, L. Jiang, and G. Cao, "ZnO cathode buffer layers for inverted polymer solar cells," *Energy & Environmental Science*, vol. 8, no. 12, pp. 3442–3476, 2015.

[33] M. A. K. Purbayanto, E. Nurfani, O. Chichvarina, J. Ding, A. Rusydi, and Y. Darma, "Oxygen vacancy enhancement promoting strong green emission through surface modification in ZnO thin film," *Applied Surface Science*, vol. 462, pp. 466–470, 2018.

[34] P. K. Mishra, S. Ayaz, T. Srivastava et al., "Role of Ga-substitution in ZnO on defect states, carrier density, mobility and UV sensing," *Journal of Materials Science: Materials in Electronics*, vol. 30, no. 20, pp. 18686–18695, 2019.

[35] V. Babentsov and R. B. James, "Anion vacancies in II–VI chalcogenides: review and critical analysis," *Journal of Crystal Growth*, vol. 379, pp. 21–27, 2013.

[36] A. A. Sokol, S. A. French, S. T. Bromley, C. R. A. Catlow, H. J. J. van Dam, and P. Sherwood, "Point defects in ZnO," *Faraday Discussions*, vol. 134, pp. 267–282, 2007.

[37] S. Vempati, J. Mitra, and P. Dawson, "One-step synthesis of ZnO nanosheets: a blue-white fluorophore," *Nanoscale Research Letters*, vol. 7, no. 1, p. 470, 2012.

[38] M. Hartel, S. Chen, B. Swerdlow et al., "Defect-induced loss mechanisms in polymer–inorganic planar heterojunction solar cells," *ACS Applied Materials & Interfaces*, vol. 5, no. 15, pp. 7215–7218, 2013.

[39] S. Bai, Z. Wu, X. Xu et al., "Inverted organic solar cells based on aqueous processed ZnO interlayers at low temperature," *Applied Physics Letters*, vol. 100, no. 20, p. 203906, 2012.

[40] P. Adhikary, S. Venkatesan, N. Adhikari et al., "Enhanced charge transport and photovoltaic performance of PBDTTT-C-T/PC70BM solar cells via UV–ozone treatment," *Nano-scale.*, vol. 5, no. 20, pp. 10007–10013, 2013.

[41] D. Li, W. Qin, S. Zhang et al., "Effect of UV-ozone process on the ZnO interlayer in the inverted organic solar cells," *RSC Advances*, vol. 7, no. 10, pp. 6040–6045, 2017.

[42] E. Polydorou, A. Zeniou, D. Tsikritzis et al., "Surface passivation effect by fluorine plasma treatment on ZnO for efficiency and lifetime improvement of inverted polymer solar cells," *Journal of Materials Chemistry A*, vol. 4, no. 30, pp. 11844–11858, 2016.

[43] V. Papamakarios, E. Polydorou, A. Soultati et al., "Surface modification of ZnO layers via hydrogen plasma treatment for efficient inverted polymer solar cells," *ACS Applied Materials & Interfaces*, vol. 8, no. 2, pp. 1194–1205, 2016.

[44] S. Zhou, J. Zhao, L. Nian et al., "High performance ZnO cathode interface doped by organic electrolyte and inorganic metal ion for organic solar cells," *Optical Materials*, vol. 109, article 110243, 2020.

[45] S. Trost, K. Zilberberg, A. Behrendt et al., "Overcoming the "light-soaking" issue in inverted organic solar cells by the use of Al:ZnO electron extraction layers," *Advanced Energy Materials*, vol. 3, no. 11, pp. 1437–1444, 2013.

[46] G. Bagha, H. Naffakh-Moosavy, and M. R. Mersagh, "The effect of reduced graphene oxide sheet on the optical and electrical characteristics of Ni-doped and ag-doped ZnO ETLs in planar perovskite solar cells," *Journal of Alloys and Compounds*, vol. 870, article 159658, 2021.

[47] F. Dabir, H. Esfahani, F. Bakhtiargonbadi, and Z. Khodadadi, "Study on microstructural and electro-optical properties of sol–gel derived pure and Al/cu-doped ZnO thin films," *Journal of Sol-Gel Science and Technology*, vol. 96, no. 3, pp. 529–538, 2020.

[48] J. W. Spalenka, P. Gopalan, H. E. Katz, and P. G. Evans, "Electron mobility enhancement in ZnO thin films via surface modification by carboxylic acids," *Applied Physics Letters*, vol. 102, no. 4, article 041602, 2013.

[49] S. Bai, Y. Jin, X. Liang et al., "Ethanedithiol treatment of solution-processed ZnO thin films: controlling the Intragap states of electron transporting interlayers for efficient and stable inverted organic photovoltaics," *Advanced Energy Materials*, vol. 5, no. 5, article 1401606, 2015.

[50] S. Yang and H. Yu, "The modification of ZnO surface with natural antioxidants to fabricate highly efficient and stable inverted organic solar cells," *Chemical Engineering Journal*, vol. 452, article 139658, 2023.

[51] V. V. Khomyak, M. M. Slyotov, I. I. Shtepliuk et al., "Annealing effect on the near-band edge emission of ZnO," *Journal of Physics and Chemistry of Solids*, vol. 74, no. 2, pp. 291–297, 2013.

[52] T.-W. Chen, C.-C. Chang, Y.-T. Hsiao et al., "Single-junction organic solar cell containing a fluorinated heptacyclic carbazole-based ladder-type acceptor affords over 13% efficiency with solution-processed cross-linkable fullerene as an interfacial layer," *ACS Applied Materials & Interfaces*, vol. 11, no. 34, pp. 31069–31077, 2019.

[53] H. Zhou, L. Zhang, X. Ma et al., "Approaching 18% efficiency of ternary layer-by-layer polymer solar cells with alloyed acceptors," *Chemical Engineering Journal*, vol. 462, article 142327, 2023.

[54] X. Ma, W. Xu, Z. Liu et al., "Over 18.1% efficiency of layer-by-layer polymer solar cells by enhancing exciton utilization near the ITO electrode," *ACS Applied Materials & Interfaces*, vol. 15, pp. 7247–7254, 2023.

[55] R. Giridharagopal and D. S. Ginger, "Characterizing morphology in bulk heterojunction organic photovoltaic systems," *Journal of Physical Chemistry Letters*, vol. 1, no. 7, pp. 1160–1169, 2010.

[56] L. Duan, N. K. Elumalai, Y. Zhang, and A. Uddin, "Progress in non-fullerene acceptor based organic solar cells," *Solar Energy Materials & Solar Cells*, vol. 193, pp. 22–65, 2019.

[57] K. Zhou, Y. Liu, A. Alotaibi et al., "Molecular and energetic order dominate the photocurrent generation process in organic solar cells with small energetic offsets," *ACS Energy Letters*, vol. 5, no. 2, pp. 589–596, 2020.

[58] L. Chen, Z. Hong, G. Li, and Y. Yang, "Recent progress in polymer solar cells: manipulation of polymer:fullerene morphology and the formation of efficient inverted polymer solar cells," *Advanced Materials*, vol. 21, no. 14-15, pp. 1434–1449, 2009.

[59] F. Padinger, R. S. Rittberger, and N. S. Sariciftci, "Effects of postproduction treatment on plastic solar cells," *Advanced Functional Materials*, vol. 13, no. 1, pp. 85–88, 2003.

[60] G. Dennler, M. C. Scharber, and C. J. Brabec, "Polymer-fullerene bulk-heterojunction solar cells," *Advanced Materials*, vol. 21, no. 13, pp. 1323–1338, 2009.

[61] S. Wakim, S. Beaupré, N. Blouin et al., "Highly efficient organic solar cells based on a poly(2,7-carbazole) derivative," *Journal of Materials Chemistry*, vol. 19, no. 30, p. 5351, 2009.

[62] T.-Y. Chu, S. Alem, S.-W. Tsang et al., "Morphology control in polycarbazole based bulk heterojunction solar cells and its impact on device performance," *Applied Physics Letters*, vol. 98, no. 25, pp. 11–14, 2011.

[63] Z. Ma, Z. Tang, E. Wang, M. R. Andersson, O. Inganäs, and F. Zhang, "Influences of surface roughness of ZnO electron transport layer on the photovoltaic performance of organic inverted solar cells," *Journal of Physical Chemistry C*, vol. 116, no. 46, pp. 24462–24468, 2012.

[64] H. Bin, Y. Yang, Z. Peng et al., "Effect of alkylsilyl side-chain structure on photovoltaic properties of conjugated polymer donors," *Advanced Energy Materials*, vol. 8, no. 8, p. 1702324, 2018.

[65] T. Ameri, J. Min, N. Li et al., "Performance enhancement of the P3HT/PCBM solar cells through NIR sensitization using a small-bandgap polymer," *Advanced Energy Materials*, vol. 2, no. 10, pp. 1198–1202, 2012.

[66] I. Horcas, R. Fernández, J. M. Gómez-Rodríguez, J. Colchero, J. Gómez-Herrero, and A. M. Baro, "WSXM: a software for scanning probe microscopy and a tool for nanotechnology," *The Review of Scientific Instruments*, vol. 78, no. 1, article 013705, 2007.

[67] M. Burgelman, P. Nollet, and S. Degrave, "Modelling polycrystalline semiconductor solar cells," *Thin Solid Films*, vol. 361-362, pp. 527–532, 2000.

[68] S. Selberherr, *Analysis and Simulation of Semiconductor Devices*, Springer Vienna, Vienna, 1ed edition, 1984.

[69] M. N. Zidan, T. Ismail, and I. S. Fahim, "Effect of thickness and temperature on flexible organic P3HT:PCBM solar cell performance," *Materials Research Express*, vol. 8, no. 9, article 095508, 2021.

[70] M. Kumar Das, S. Panda, and N. Mohapatra, "Power conversion efficiency optimization of LaFeO3 Mott insulator based solar cell with metal oxide transport layers using SCAPS," *Materials Today: Proceedings*, vol. 74, pp. 756–762, 2023.

[71] T. Kirchartz, B. E. Pieters, J. Kirkpatrick, U. Rau, and J. Nelson, "Recombination via tail states in polythiophene:-fullerene solar cells," *Physical Review B*, vol. 83, no. 11, p. 115209, 2011.

[72] E. Zakhidov, M. Imomov, V. Quvondikov et al., "Comparative study of absorption and photoluminescent properties of organic solar cells based on P3HT:PCBM and P3HT:ITIC blends," *Applied Physics A: Materials Science & Processing*, vol. 125, no. 11, p. 803, 2019.

[73] W. Abdelaziz, A. Shaker, M. Abouelatta, and A. Zekry, "Possible efficiency boosting of non-fullerene acceptor solar cell using device simulation," *Optical Materials*, vol. 91, pp. 239–245, 2019.

[74] N. Gasparini, M. Salvador, T. Heumueller et al., "Polymer:nonfullerene bulk heterojunction solar cells with exceptionally low recombination rates," *Advanced Energy Materials*, vol. 7, no. 22, article 1701561, 2017.

[75] N. Gasparini, A. Wadsworth, M. Moser, D. Baran, I. McCulloch, and C. J. Brabec, "The physics of small molecule acceptors for efficient and stable bulk heterojunction solar cells," *Advanced Energy Materials*, vol. 8, no. 12, p. 1703298, 2018.

[76] H. Li, C. J. Firby, and A. Y. Elezzabi, "Rechargeable aqueous hybrid Zn2+/Al3+ electrochromic batteries," *Joule*, vol. 3, pp. 2268–2278, 2019.

[77] D. M. Bezerra and J. E. F. S. Rodrigues, "Structural, vibrational and morphological properties of layered double hydroxides containing Ni2+, Zn2+, Al3+ and Zr4+ cations," *Materials Characterization*, vol. 125, pp. 29–36, 2017.

[78] Y. Bouachiba, A. Mammeri, A. Bouabellou et al., "Optoelectronic and birefringence properties of weakly Mg-doped ZnO thin films prepared by spray pyrolysis," *Journal of Materials Science: Materials in Electronics*, vol. 33, no. 9, pp. 6689–6699, 2022.

[79] U. Holzwarth and N. Gibson, "The Scherrer equation versus the "Debye-Scherrer equation,"" *Nature Nanotechnology*, vol. 6, no. 9, pp. 534–534, 2011.

[80] K. He, N. Chen, C. Wang, L. Wei, and J. Chen, "Method for determining crystal grain size by X-ray diffraction," *Crystal Research and Technology*, vol. 53, no. 2, p. 1700157, 2018.

[81] K. Vanheusden, C. H. Seager, W. L. Warren, D. R. Tallant, and J. A. Voigt, "Correlation between photoluminescence and oxygen vacancies in ZnO phosphors," *Applied Physics Letters*, vol. 68, no. 3, pp. 403–405, 1996.

[82] F. Leiter, H. Zhou, F. Henecker, A. Hofstaetter, D. M. Hofmann, and B. K. Meyer, "Magnetic resonance experiments on the green emission in undoped ZnO crystals," *Physica B: Condensed Matter*, vol. 308-310, pp. 908–911, 2001.

[83] S. Nadupalli, S. Repp, S. Weber, and E. Erdem, "About defect phenomena in ZnO nanocrystals," *Nano-scale.*, vol. 13, no. 20, pp. 9160–9171, 2021.

[84] Z. Wu, H. Yu, S. Shi, and Y. Li, "Bismuth oxysulfide modified ZnO nanorod arrays as an efficient electron transport layer for inverted polymer solar cells," *Journal of Materials Chemistry A*, vol. 7, no. 24, pp. 14776–14789, 2019.

[85] J. Tauc and A. Menth, "States in the gap," *Journal of Non-Crystalline Solids*, vol. 8-10, pp. 569–585, 1972.

[86] V. Mote, Y. Purushotham, and B. Dole, "Williamson-Hall analysis in estimation of lattice strain in nanometer-sized ZnO particles," *Journal of Theoretical and Applied Physics*, vol. 6, no. 1, p. 6, 2012.

[87] J. R. Macdonald, "Impedance spectroscopy and its use in analyzing the steady-state AC response of solid and liquid

electrolytes," *Journal of Electroanalytical Chemistry and Interfacial Electrochemistry*, vol. 223, no. 1-2, pp. 25–50, 1987.

[88] T. Kuwabara, C. Iwata, T. Yamaguchi, and K. Takahashi, "Mechanistic insights into UV-induced electron transfer from PCBM to titanium oxide in inverted-type organic thin film solar cells using AC impedance spectroscopy," *ACS Applied Materials & Interfaces*, vol. 2, no. 8, pp. 2254–2260, 2010.

[89] B. Conings, L. Baeten, H.-G. Boyen et al., "Influence of interface morphology onto the photovoltaic properties of nano-patterned ZnO/poly(3-hexylthiophene) hybrid solar cells. An impedance spectroscopy study," *The Journal of Physical Chemistry C*, vol. 115, pp. 16695–16700, 2011.

[90] H. Woo Lee, J. Young Oh, T. Il Lee et al., "Highly efficient inverted polymer solar cells with reduced graphene-oxide-zinc-oxide nanocomposites buffer layer," *Applied Physics Letters*, vol. 102, no. 19, article 193903, 2013.

[91] P. Li, L. Cai, G. Wang et al., "PEIE capped ZnO as cathode buffer layer with enhanced charge transfer ability for high efficiency polymer solar cells," *Synthetic Metals*, vol. 203, pp. 243–248, 2015.

[92] Y. Zhang, L. Li, S. Yuan, G. Li, and W. Zhang, "Electrical properties of the interfaces in bulk heterojunction organic solar cells investigated by electrochemical impedance spectroscopy," *Electrochimica Acta*, vol. 109, pp. 221–225, 2013.

[93] A. Kumar, D. K. Jarwal, A. K. Mishra et al., "Synergistic effect of CdSe quantum dots (QDs) and PC61BM on ambient-air processed ZnO QDs/PCDTBT: PC61BM:CdSe QDs/MoO3-based ternary organic solar cells," *Nanotechnology*, vol. 31, no. 46, article 465404, 2020.

[94] W. Huang, X. Zhuang, F. S. Melkonyan et al., "UV–ozone interfacial modification in organic transistors for high-sensitivity NO2detection," *Advanced Materials*, vol. 29, no. 31, article 1701706, 2017.

[95] K. Jung, D. H. Kim, J. Kim et al., "Influence of a UV-ozone treatment on amorphous SnO2 electron selective layers for highly efficient planar MAPbI3 perovskite solar cells," *Journal of Materials Science and Technology*, vol. 59, pp. 195–202, 2020.

[96] R. J. Good and L. A. Girifalco, "A theory for estimation of surface and interfacial energies. III. Estimation of surface energies of solids from contact angle data," *The Journal of Physical Chemistry A*, vol. 64, pp. 561–565, 1960.

[97] Y.-J. Lee, J. Wang, S. R. Cheng, and J. W. P. Hsu, "Solution processed ZnO hybrid nanocomposite with tailored work function for improved electron transport layer in organic photovoltaic devices," *ACS Applied Materials & Interfaces*, vol. 5, no. 18, pp. 9128–9133, 2013.

[98] H. Bin, L. Gao, Z.-G. Zhang et al., "11.4% Efficiency non-fullerene polymer solar cells with trialkylsilyl substituted 2D-conjugated polymer as donor," *Nature Communications*, vol. 7, p. 13651, 2016.

[99] Y. Ma, X. Zhou, D. Cai, Q. Tu, W. Ma, and Q. Zheng, "A minimal benzo[c][1,2,5]thiadiazole-based electron acceptor as a third component material for ternary polymer solar cells with efficiencies exceeding 16.0%," *Materials Horizons Journal*, vol. 7, pp. 117–124, 2020.

[100] B. Qi and J. Wang, "Fill factor in organic solar cells," *Physical Chemistry Chemical Physics*, vol. 15, no. 23, p. 8972, 2013.

[101] M.-H. Jao, H.-C. Liao, and W.-F. Su, "Achieving a high fill factor for organic solar cells," *Journal of Materials Chemistry A*, vol. 4, no. 16, pp. 5784–5801, 2016.

[102] S. B. Hacène and T. Benouaz, "Influence of charge carrier mobility and surface recombination velocity on the characteristics of P3HT:PCBM organic solar cells," *Physica Status Solidi*, vol. 211, no. 4, pp. 862–868, 2014.

[103] C.-T. Sah and W. Shockley, "Electron-hole recombination statistics in semiconductors through flaws with many charge conditions," *Physics Review*, vol. 109, no. 4, pp. 1103–1115, 1958.

[104] R. C. I. MacKenzie, T. Kirchartz, G. F. A. Dibb, and J. Nelson, "Modeling nongeminate recombination in P3HT:PCBM solar cells," *Journal of Physical Chemistry C*, vol. 115, no. 19, pp. 9806–9813, 2011.

[105] H. Sun, F. Chen, and Z.-K. Chen, "Recent progress on non-fullerene acceptors for organic photovoltaics," *Materials Today*, vol. 24, pp. 94–118, 2019.